Title
An Analytical Algorithm for Tensor Tomography From Projections Acquired About Three Axes

Journal
IEEE Transactions on Medical Imaging, 41(11)

ISSN
0278-0062

Authors
Tao, Weijie
Rohmer, Damien
Gullberg, Grant T
et al.

Publication Date
2022-11-01

DOI
10.1109/tmi.2022.3186983

Peer reviewed

An Analytical Algorithm for Tensor Tomography From Projections Acquired About Three Axes

Weijie Tao, Damien Rohmer, Grant T. Gullberg, *Life Fellow, IEEE*, Youngho Seo, *Senior Member, IEEE*, and Qiu Huang, *Member, IEEE*

***Abstract*— Tensor fields are useful for modeling the structure of biological tissues. The challenge to measure tensor fields involves acquiring sufficient data of scalar measurements that are physically achievable and reconstructing tensors from as few projections as possible for efficient applications in medical imaging. In this paper, we present a filtered back-projection algorithm for the reconstruction of a symmetric second-rank tensor field from directional X-ray projections about three axes. The tensor field is decomposed into a solenoidal and irrotational component, each of three unknowns. Using the Fourier projection theorem, a filtered back-projection algorithm is derived to reconstruct the solenoidal and irrotational components from projections acquired around three axes. A simple illustrative phantom consisting of two spherical shells and a 3D digital cardiac diffusion image obtained from diffusion tensor MRI of an excised human heart are used to simulate directional X-ray projections. The simulations validate the mathematical derivations and demonstrate reasonable noise properties of the algorithm. The decomposition of the tensor field into solenoidal and irrotational components provides insight into the development of algorithms for reconstructing tensor fields with sufficient samples in terms of the type of directional projections and the necessary orbits for the acquisition of the projections of the tensor field.**

***Index Terms*— Filtered back-projection algorithm, solenoidal and irrotational components, tensor tomography, directional X-ray projections.**

I. Introduction

TENSOR tomography has found important applications in the physical sciences [1], [2], mathematics [3], and medicine [4]. Here we consider the tensor tomography problem as the reconstruction of symmetric second-rank tensor fields. The work aims to develop acquisition schemes and filtered back-projection algorithms for the three-dimensional reconstruction of the six unknown tensor elements.

In medicine, one application of tensors is to model the biological structure by using X-ray imaging of small-angle scatter to characterize in vivo fiber structures of lung [5], bone [6], and breast [7]. The small-angle scatter captured by X-ray dark-field imaging is orientation dependent [8]–[15] and as such is not captured in regular 3D X-ray tomography. Thus, in many studies of X-ray dark-field imaging, the question arises as to whether sufficient data is obtained to uniquely reconstruct the tensor models used to represent the small-angle scatter. Another important medical application is using tensors to model the helical fiber structure of cardiac muscle [16] using MRI diffusion imaging [17], [18]. Understanding the 3D fiber structure of the heart is essential for modeling the mechanical and electrical properties; changes in the fiber configuration may be of significant importance to understand the remodeling in the progression to heart failure [19] and after myocardial infarction [20]. Currently, most MR diffusion tensor imaging (DTI) studies require a very large number of signal measurements, whereas the focus here is to develop tensor tomographic techniques that might provide faster and more accurate data acquisitions.

The tensor tomographic problem is an extension of the vector tomographic problem [21]–[36] and draws on much of the work in the reconstruction of vector fields (first-rank tensor fields) [31], [35]; in particular, the decomposition of the tensor field into solenoidal and irrotational components [3], [37]–[40] and the extension of the Fourier projection theorem from scalar and vector fields [32], [35] to tensor fields [37]–[40]. This decomposition provides a formulation to analyze data acquisition schemes and reconstruction algorithms from the mathematical construction of projections that might simplify the data acquisition yet provide accurate and precise reconstruction results.

The present work is stimulated by papers [41]–[43], where it was shown that rotations about at least three orthogonal axes are necessary to reconstruct 3D symmetric second-rank tensor fields. They developed explicit plane-by-plane filtered back-projection reconstruction algorithms using six sets of projections obtained by rotating about three orthogonal axes: three sets of scalar projection measurements for diagonal

Manuscript received 3 April 2022; revised 17 June 2022; accepted 22 June 2022. Date of publication 1 July 2022; date of current version 27 October 2022. This work was supported in part by the China Scholarship Council under Grant 201906230215 and in part by the National Institutes of Health under Grant R43 EB027535, Grant R01 EB026331, and Grant R01 HL135490. *(Corresponding author: Qiu Huang.)*

Weijie Tao and Qiu Huang are with the Department of Nuclear Medicine, Ruijin Hospital, School of Medicine, Shanghai Jiao Tong University, Shanghai 200240, China, and also with the School of Biomedical Engineering, Shanghai Jiao Tong University, Shanghai 200240, China (e-mail: qiuhuang@sjtu.edu.cn).

Damien Rohmer is with the Geometric and Visual Computing (GeoViC) Research Team, Ecole Polytechnique/CNRS, Institut Polytechnique de Paris, 91120 Palaiseau, France.

Grant T. Gullberg and Youngho Seo are with the Department of Radiology, University of California San Francisco, San Francisco, CA 94143 USA.

Digital Object Identifier 10.1109/TMI.2022.3186983

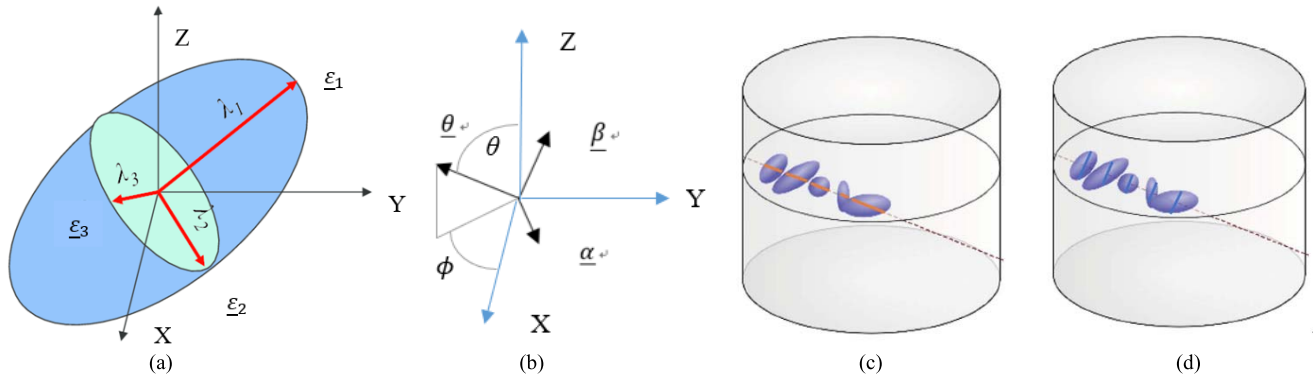

Fig. 1. (a) A second rank tensor illustrated as an ellipsoid. The eigenvectors $\underline{\varepsilon}_1$, $\underline{\varepsilon}_2$, $\underline{\varepsilon}_3$ of the tensor are the 3-unit vectors along the principal semi-axes of the ellipsoid, and the eigenvalues $\lambda_1, \lambda_2, \lambda_3 \geq 0$ are the lengths of the principal semi-axes. (Drawn based on Fig. 5 in [46]) (b) Three orthogonal vectors $\underline{\theta}$, $\underline{\alpha}$, $\underline{\beta}$, with zenith angle θ and azimuth angle ϕ, for the directional X-ray transform. (c) $p_{\underline{\theta}}^{\underline{\theta}\,\underline{\theta}}$: the integral along $\underline{\theta}$ of the orange intersections (along $\underline{\theta}$). (d) $p_{\underline{\theta}}^{\underline{\beta}\,\underline{\beta}}$: the integral along $\underline{\theta}$ of the blue intersections (along $\underline{\beta}$). Here the integration line goes through the center of all ellipsoids. (Drawn based on Fig. 5 in [46] but modified to indicate the tensor measurements along $\underline{\theta}$ and $\underline{\beta}$.)

components, and three for off-diagonal components. It has also been shown for slice-by-slice vector field tomography in [33], [34], [36] that three perpendicular axes are sufficient for a full recovery. Our approach is to separate the tensor field into solenoidal and irrotational components [37]–[40], [44] so that one set of three directional measurements around three axes reconstructs the solenoidal component of the tensor field; and the reconstructed solenoidal component along with a different set of three directional measurements about the same axes reconstructs the irrotational component.

In the following sections, we first present the definitions and notations used in our work, including the formulation for the decomposition of a symmetric second-rank tensor field into solenoidal and irrotational components. From this decomposition, we derive the algorithm for reconstructing the tensor field from measurements around three axes that involve a reconstruction of the solenoidal component and another reconstruction of the irrotational component. In the section of Implementation, we describe how the scalar projections of the tensor fields are simulated for two phantoms. Then we assess the reconstructions and compare results at different noise levels. This is followed by a discussion of the advantages of tensor tomography.

II. Definitions and Notations

In this work, we use the Fourier projection theorem to show that the Fourier transform of the X-ray projections is related to the Fourier transform of the solenoidal and irrotational components of the second-rank symmetric tensor field.

A. 3D Second-Rank Tensor Field and Its X-Ray Transform

For a point $\underline{x} = (x, y, z)^T$ in $\Re^3$, the 3D second-rank tensor $T(\underline{x})$ is denoted by its nine real elements that are rapidly decreasing C^∞ functions:

$$T(\underline{x}) = \begin{bmatrix} t_{xx} & t_{xy} & t_{xz} \\ t_{yx} & t_{yy} & t_{yz} \\ t_{zx} & t_{zy} & t_{zz} \end{bmatrix} (\underline{x}) . \tag{1}$$

As shown in Fig. 1(a), the tensor field can be illustrated as an ellipsoid [45], where the eigenvectors $\underline{\varepsilon}_1$, $\underline{\varepsilon}_2$, $\underline{\varepsilon}_3$ of the tensor are the three unit vectors along the principal semi-axes of the ellipsoid, and the corresponding eigenvalues λ_1, λ_2, λ_3 greater than or equal to zero are lengths of the principal semi-axes.

Similar to the X-ray transform for a scalar image, the directional X-ray transform of a tensor field is defined here as the line integral of the tensor field along a specific direction $\underline{\theta}$ for a zenith angle θ and an azimuth angle ϕ (Fig. 1(b)) [40]:

$$p_{\underline{\theta}}^{\underline{a}\,\underline{b}}(u, v) = \int_{-\infty}^{\infty} \underline{a}^T T\left(t\underline{\theta} + u\underline{\alpha} + v\underline{\beta}\right) \underline{b} dt, \tag{2}$$

where the three orthogonal vectors are defined as

$$\begin{aligned} \underline{\theta} &= (sin\theta cos\phi, sin\theta sin\phi, cos\theta)^T , \\ \underline{\alpha} &= (-sin\phi, cos\phi, 0)^T , \\ \underline{\beta} &= (-cos\theta cos\phi, -cos\theta sin\phi, sin\theta)^T . \end{aligned} \tag{3}$$

Equation (2) is the directional projection measurement defined by the 3D directional unit vectors $\underline{a}$ and $\underline{b}$. In this paper, we will use directional X-ray projections measured with $\underline{a} = \underline{b} = \underline{\theta}$ and $\underline{a} = \underline{b} = \underline{\beta}$, namely $p_{\underline{\theta}}^{\underline{\theta}\,\underline{\theta}}$ and $p_{\underline{\theta}}^{\underline{\beta}\,\underline{\beta}}$. The projection $p_{\underline{\theta}}^{\underline{\theta}\,\underline{\theta}}$ usually refers to the longitudinal measurement, i.e., direct projection of the vector or tensor field along the line of projection, and the projection $p_{\underline{\theta}}^{\underline{\beta}\,\underline{\beta}}$ refers to the transverse projection measurements. For MRI diffusion imaging these projections are easy to measure with the pulse sequence implementation of the diffusion gradients. It is impossible to implement with $\underline{a} = \underline{\theta}$, $\underline{b} = \underline{\alpha}$. These measurements have to be performed using a combination of $\underline{a} = \underline{b} = \underline{\theta}_1$ and $\underline{a} = \underline{b} = \underline{\theta}_2$ (see reference [38]). Likewise, for X-ray interferometry $p_{\underline{\theta}}^{\underline{\theta}\,\underline{\theta}}$ provides the dark-field projections of the longitudinal measurements of the small-angle scatter, and $p_{\underline{\theta}}^{\underline{\beta}\,\underline{\beta}}$ provides the projection of the transverse measurements that correspond to the sensitivity direction of the gratings in the measurement of dark-field projections. The angle $\underline{a} = \underline{b} = \underline{\theta}$,

and the angle $\underline{a} = \underline{b} = \underline{\beta}$ were chosen following the angles selected in Lionheart's paper [43].

The projection $p_{\underline{\theta}}^{\underline{\theta}\,\underline{\theta}}$ indicates the integral in the direction of $\underline{\theta}$ (indicated by the subscript $\underline{\theta}$) of the tensor field along the orange line presented in Fig. 1(c). The ellipsoids are a pictorial representation of the tensor at each voxel. In this case the contribution of each voxel to the line integral is the length of the orange line intersecting the ellipsoid. Whereas, for the projection $p_{\underline{\theta}}^{\underline{\beta}\,\underline{\beta}}$ presented in Fig. 1(d), the contribution of each pixel to the line integral in the direction of $\underline{\theta}$ is the length of the blue line in the direction of $\underline{\beta}$ intersecting the ellipsoid.

B. Fourier Projection Theorem for X-Ray Projections

In this section, we introduce the Fourier projection theorem for tensor fields, which is a straightforward extension of the Fourier slice theorem for vector fields [31], [32], [35].

The Fourier transform of $p_{\underline{\theta}}^{\underline{a}\,\underline{b}}(u, v)$ is defined as

$$\tilde{p}_{\underline{\theta}}^{\underline{a}\,\underline{b}}(\nu_u, \nu_v) = \int_{-\infty}^{\infty}\int_{-\infty}^{\infty} p_{\underline{\theta}}^{\underline{a}\,\underline{b}}(u, v)\, e^{-2\pi i(u\nu_u + v\nu_v)}\mathrm{d}u\mathrm{d}v. \quad (4)$$

Substituting the definition in (2) into (4), one obtains

$$\tilde{p}_{\underline{\theta}}^{\underline{a}\,\underline{b}}(\nu_u, \nu_v) = \int_{-\infty}^{\infty}\int_{-\infty}^{\infty}\int_{-\infty}^{\infty} \underline{a}^T T\left(t\underline{\theta} + u\underline{\alpha} + v\underline{\beta}\right)\underline{b}\,dt\, e^{-2\pi i(u\nu_u + v\nu_v)}\mathrm{d}u\mathrm{d}v.$$

With the change of variables $\underline{x} = t\underline{\theta} + u\underline{\alpha} + v\underline{\beta}$, it can be rewritten as

$$\tilde{p}_{\underline{\theta}}^{\underline{a}\,\underline{b}}(\nu_u, \nu_v) = \int_{-\infty}^{\infty}\int_{-\infty}^{\infty}\int_{-\infty}^{\infty} \underline{a}^T T(\underline{x})\,\underline{b}\, e^{-2\pi i\left(\underline{x}\,\underline{\alpha}\nu_u + \underline{x}\,\underline{\beta}\nu_v\right)} d\underline{x}.$$

This leads to the following formulation of the Fourier projection theorem for the projection in the direction of $\underline{\theta}$:

$$\tilde{p}_{\underline{\theta}}^{\underline{a}\,\underline{b}}(\nu_u, \nu_v) = \underline{a}^T \tilde{T}\left(\underline{\alpha}\nu_u + \underline{\beta}\nu_v\right)\underline{b}, \quad (5)$$

where $\tilde{T}\left(\underline{\alpha}\nu_u + \underline{\beta}\nu_v\right)$ is the three-dimensional Fourier transform of the tensor $T(\underline{x})$ and $\underline{\alpha}\nu_u + \underline{\beta}\nu_v = \underline{\nu} = [\nu_x, \nu_y, \nu_z]^T$.

C. Tensor Field Decomposition

We only consider the reconstruction of a symmetric tensor field here in this work, which reduces unknown elements from 9 to 6. It was shown by Sharafutdinov [47] that any sufficiently smooth symmetric tensor field vanishing rapidly at infinity can be decomposed in a unique way to a solenoidal component $T_\Psi^S(\underline{x})$ and an irrotational component $T_\Phi^I(\underline{x})$:

$$T(\underline{x}) = T_\Psi^S(\underline{x}) + T_\Phi^I(\underline{x}), \quad (6)$$

where the solenoidal component $T_\Psi^S(\underline{x})$ is a symmetric tensor and is divergence free; and the irrotational component $T_\Phi^I(\underline{x})$ is a symmetric tensor. Further, we specify the solenoidal component as a curl of a tensor potential that has to be applied to each column of Ψ (Appendix):

$$T_\Psi^S(\underline{x}) = \nabla \times \Psi(\underline{x}), \quad (7)$$

with the tensor potential defined as

$$\Psi(\underline{x}) = \begin{bmatrix} 0 & \frac{\partial X_1}{\partial z} & -\frac{\partial X_1}{\partial y} \\ -\frac{\partial X_2}{\partial z} & 0 & \frac{\partial X_2}{\partial x} \\ \frac{\partial X_3}{\partial y} & -\frac{\partial X_3}{\partial x} & 0 \end{bmatrix}(\underline{x}) \quad (8)$$

for three scalar functions $X_1(\underline{x})$, $X_2(\underline{x})$, $X_3(\underline{x})$. Substituting (8) into (7), the solenoidal component is

$$T_\Psi^S(\underline{x}) = \begin{bmatrix} \frac{\partial^2 X_3}{\partial y^2} + \frac{\partial^2 X_2}{\partial z^2} & -\frac{\partial^2 X_3}{\partial y \partial x} & -\frac{\partial^2 X_2}{\partial z \partial x} \\ -\frac{\partial^2 X_3}{\partial x \partial y} & \frac{\partial^2 X_1}{\partial z^2} + \frac{\partial^2 X_3}{\partial x^2} & -\frac{\partial^2 X_1}{\partial z \partial y} \\ -\frac{\partial^2 X_2}{\partial x \partial z} & -\frac{\partial^2 X_1}{\partial y \partial z} & \frac{\partial^2 X_2}{\partial x^2} + \frac{\partial^2 X_1}{\partial y^2} \end{bmatrix}(\underline{x}). \quad (9)$$

The irrotational component in (6) is the gradient of a vector potential:

$$T_\Phi^I(\underline{x}) = \nabla\underline{\Phi}(\underline{x}) + \left[\nabla\underline{\Phi}(\underline{x})\right]^T, \quad (10)$$

with the vector potential defined as

$$\underline{\Phi}(\underline{x}) = \begin{bmatrix} \Phi_1 \\ \Phi_2 \\ \Phi_3 \end{bmatrix}(\underline{x}) \quad (11)$$

for three scalar functions $\Phi_1(\underline{x})$, $\Phi_2(\underline{x})$, and $\Phi_3(\underline{x})$. Using (10) and (11), the irrotational component is

$$T_\Phi^I(\underline{x}) = \begin{bmatrix} 2\frac{\partial \Phi_1}{\partial x} & \frac{\partial \Phi_1}{\partial y} + \frac{\partial \Phi_2}{\partial x} & \frac{\partial \Phi_1}{\partial z} + \frac{\partial \Phi_3}{\partial x} \\ \frac{\partial \Phi_1}{\partial y} + \frac{\partial \Phi_2}{\partial x} & 2\frac{\partial \Phi_2}{\partial y} & \frac{\partial \Phi_2}{\partial z} + \frac{\partial \Phi_3}{\partial y} \\ \frac{\partial \Phi_1}{\partial z} + \frac{\partial \Phi_3}{\partial x} & \frac{\partial \Phi_2}{\partial z} + \frac{\partial \Phi_3}{\partial y} & 2\frac{\partial \Phi_3}{\partial z} \end{bmatrix}(\underline{x}). \quad (12)$$

With (9) and (12), the Fourier transform of the solenoidal and irrotational components at $\underline{\nu} = (\nu_x, \nu_y, \nu_z)^T$ can be written in terms of the Fourier transforms of X_1, X_2, X_3, Φ_1, Φ_2 and Φ_3:

According to the decomposition in (6), the Fourier projection theorem (5) becomes:

$$\tilde{p}_{\underline{\theta}}^{\underline{a}\,\underline{b}}(\nu_u, \nu_v) = \underline{a}^T \tilde{T}_\Psi^S\left(\underline{\alpha}\nu_u + \underline{\beta}\nu_v\right)\underline{b} + \underline{a}^T \tilde{T}_\Phi^I\left(\underline{\alpha}\nu_u + \underline{\beta}\nu_v\right)\underline{b}$$

With $\underline{a} = \underline{b} = \underline{\theta}$ and $\underline{a} = \underline{b} = \underline{\beta}$, we have

$$\tilde{p}_{\underline{\theta}}^{\underline{\theta}\,\underline{\theta}}(\nu_u, \nu_v) = \underline{\theta}^T \tilde{T}_\Psi^S\left(\underline{\alpha}\nu_u + \underline{\beta}\nu_v\right)\underline{\theta} + \underline{\theta}^T \tilde{T}_\Phi^I\left(\underline{\alpha}\nu_u + \underline{\beta}\nu_v\right)\underline{\theta},$$

and

$$\tilde{p}_{\underline{\theta}}^{\underline{\beta}\,\underline{\beta}}(\nu_u, \nu_v) = \underline{\beta}^T \tilde{T}_\Psi^S\left(\underline{\alpha}\nu_u + \underline{\beta}\nu_v\right)\underline{\beta} + \underline{\beta}^T \tilde{T}_\Phi^I\left(\underline{\alpha}\nu_u + \underline{\beta}\nu_v\right)\underline{\beta}.$$

Substituting (13), as shown at the bottom of the page, into these two equations, we have the solenoidal and irrotational components of $\tilde{p}_{\underline{\theta}}^{\underline{\theta}\,\underline{\theta}}$ as

$$\begin{aligned}
&\underline{\theta}^T \tilde{T}_\Psi^S \left(\underline{\alpha}\nu_u + \underline{\beta}\nu_v\right)\underline{\theta} \\
&= (\nu_u \cos\theta\cos\phi - \nu_v \sin\phi)^2 \tilde{X}_1 \left(\nu_u\underline{\alpha} + \nu_v\underline{\beta}\right) \\
&\quad + \nu_u (\cos\theta \sin\phi + \nu_v \cos\phi)^2 \tilde{X}_2 \left(\nu_u\underline{\alpha} + \nu_v\underline{\beta}\right) \\
&\quad + (\nu_u \sin\theta)^2 \tilde{X}_3 \left(\nu_u\underline{\alpha} + \nu_v\underline{\beta}\right), \qquad (14)\\
&\underline{\theta}^T \tilde{T}_\Phi^I \left(\underline{\alpha}\nu_u + \underline{\beta}\nu_v\right)\underline{\theta} = 0, \qquad (15)
\end{aligned}$$

and the solenoidal and irrotational components of $\tilde{p}_{\underline{\theta}}^{\underline{\beta}\,\underline{\beta}}$ as:

$$\begin{aligned}
&\underline{\beta}^T \tilde{T}_\Psi^S \left(\underline{\alpha}\nu_u + \underline{\beta}\nu_v\right)\underline{\beta} \\
&= (\nu_u \sin\theta\cos\phi)^2 \tilde{X}_1 \left(\nu_u\underline{\alpha} + \nu_v\underline{\beta}\right) \\
&\quad + (\nu_u \sin\theta\sin\phi)^2 \tilde{X}_2 \left(\nu_u\underline{\alpha} + \nu_v\underline{\beta}\right) \\
&\quad + (\nu_u \cos\theta)^2 \tilde{X}_3 \left(\nu_u\underline{\alpha} + \nu_v\underline{\beta}\right), \qquad (16)\\
&\underline{\beta}^T \tilde{T}_\Phi^I \left(\underline{\alpha}\nu_u + \underline{\beta}\nu_v\right)\underline{\beta} \\
&= -2\nu_v \cos\theta\cos\phi \tilde{\Phi}_1 \left(\nu_u\underline{\alpha} + \nu_v\underline{\beta}\right) \\
&\quad - 2\nu_v \cos\theta\sin\phi \tilde{\Phi}_2 \left(\nu_u\underline{\alpha} + \nu_v\underline{\beta}\right) \\
&\quad + 2\nu_v \sin\theta \tilde{\Phi}_3 \left(\nu_u\underline{\alpha} + \nu_v\underline{\beta}\right). \qquad (17)
\end{aligned}$$

III. Algorithm

We see from (14) and (15) that the directional X-ray transform $p_{\underline{\theta}}^{\underline{\theta}\,\underline{\theta}}$ is composed of only the solenoidal component containing three unknowns X_1, X_2, X_3. Thus, the solenoidal component can be reconstructed from the X-ray transform $p_{\underline{\theta}}^{\underline{\theta}\,\underline{\theta}}$ around three axes. Based on (16) and (17), we acquire $p_{\underline{\theta}}^{\underline{\beta}\,\underline{\beta}}$ around three axes (more likely the same three axes), together with solutions for X_1, X_2, X_3, to reconstruct the irrotational component.

A. Solenoidal Component Reconstruction Using $p_{\underline{\theta}}^{\underline{\theta}\,\underline{\theta}}$

For convenience, we identify projections $p_{\underline{\theta}}^{\underline{\theta}\,\underline{\theta}}$ rotating about the x, y and z axes as P_x, P_y, P_z and consider reconstructing the three unknowns X_1, X_2, X_3.

For projections acquired around the x-axis, ϕ in (3) is 90°, $\underline{\theta}_1 = (0, \sin\theta, \cos\theta)$, $\underline{\alpha}_1 = (-1, 0, 0)$, $\underline{\beta}_1 = (0, -\cos\theta, \sin\theta)$. By summing (14) and (15), we have

$$\begin{aligned}
\tilde{P}_x\left(\nu_{u_1}, \nu_{v_1}\right) &= \nu_{v_1}^2 \tilde{X}_1 \left(\nu_{u_1}\underline{\alpha}_1 + \nu_{v_1}\underline{\beta}_1\right) \\
&\quad + (\nu_{u_1}\cos\theta)^2 \tilde{X}_2 \left(\nu_{u_1}\underline{\alpha}_1 + \nu_{v_1}\underline{\beta}_1\right) \\
&\quad + (\nu_{u_1}\sin\theta)^2 \tilde{X}_3 \left(\nu_{u_1}\underline{\alpha}_1 + \nu_{v_1}\underline{\beta}_1\right). \qquad (18)
\end{aligned}$$

Similarly, for projections acquired around the y-axis, ϕ in (3) is 0°, $\underline{\theta}_2 = (\sin\theta, 0, \cos\theta)$, $\underline{\alpha}_2 = (0, 1, 0)$, $\underline{\beta}_2 = (-\cos\theta, 0, \sin\theta)$. We can write $\tilde{p}_{\underline{\theta}}^{\underline{\theta}\,\underline{\theta}}$ as:

$$\begin{aligned}
\tilde{P}_y\left(\nu_{u_2}, \nu_{v_2}\right) &= (\nu_{u_2}\cos\theta)^2 \tilde{X}_1 \left(\nu_{u_2}\underline{\alpha}_2 + \nu_{v_2}\underline{\beta}_2\right) \\
&\quad + \nu_{v_2}^2 \tilde{X}_2 \left(\nu_{u_2}\underline{\alpha}_2 + \nu_{v_2}\underline{\beta}_2\right) \\
&\quad + (\nu_{u_2}\sin\theta)^2 \tilde{X}_3 \left(\nu_{u_2}\underline{\alpha}_2 + \nu_{v_2}\underline{\beta}_2\right). \qquad (19)
\end{aligned}$$

For projections acquired around the z-axis, θ in (3) equals 90°, $\underline{\theta}_3 = (\cos\phi, \sin\phi, 0)$, $\underline{\alpha}_3 = (-\sin\phi, \cos\phi, 0)$, $\underline{\beta}_3 = (0, 0, 1)$. We have

$$\begin{aligned}
\tilde{P}_z\left(\nu_{u_3}, \nu_{v_3}\right) &= (\nu_{v_3}\sin\phi)^2 \tilde{X}_1 \left(\nu_{u_3}\underline{\alpha}_3 + \nu_{v_3}\underline{\beta}_3\right) \\
&\quad + \left(\nu_{v_3}\cos\phi\right)^2 \tilde{X}_2 \left(\nu_{u_3}\underline{\alpha}_3 + \nu_{v_3}\underline{\beta}_3\right) \\
&\quad + \nu_{u_3}^2 \tilde{X}_3 \left(\nu_{u_3}\underline{\alpha}_3 + \nu_{v_3}\underline{\beta}_3\right). \qquad (20)
\end{aligned}$$

In these three equations, the zenith angle θ and the azimuth angle ϕ are not necessarily the same, neither are vectors $\underline{\alpha}$ and $\underline{\beta}$. Hence the corresponding coefficients of the vectors, ν_v and ν_u vary according to (18) - (20). This is why we add subscripts 1, 2, 3 to indicate the difference.

To solve (18) - (20) for $\tilde{X}_1$, $\tilde{X}_2$ and $\tilde{X}_3$, we need to change their coordinates to the global coordinate system (ν_x, ν_y, ν_z) so that the three equations are sampled in the same 3D grid. With the coordinate transformation as

$$\begin{aligned}
[\nu_x, \nu_y, \nu_z]^T &= \nu_{u_1}\underline{\alpha}_1 + \nu_{v_1}\underline{\beta}_1 = [-\nu_{u_1}, -\nu_{v_1}\cos\theta, \nu_{v_1}\sin\theta]^T, \\
[\nu_x, \nu_y, \nu_z]^T &= \nu_{u_2}\underline{\alpha}_2 + \nu_{v_2}\underline{\beta}_2 = [-\nu_{v_2}\cos\theta, \nu_{u_2}, \nu_{v_2}\sin\theta]^T, \\
[\nu_x, \nu_y, \nu_z]^T &= \nu_{u_3}\underline{\alpha}_3 + \nu_{v_3}\underline{\beta}_3 = [-\nu_{u_3}\sin\phi, \nu_{u_3}\cos\phi, \nu_{v_3}]^T, \qquad (21)
\end{aligned}$$

$$\begin{aligned}
\tilde{T}_\Psi^S(\underline{\nu}) &= 2\pi i \begin{bmatrix}
\nu_y^2\tilde{X}_3(\underline{\nu}) + \nu_z^2\tilde{X}_2(\underline{\nu}) & -\nu_y\nu_x\tilde{X}_3(\underline{\nu}) & -\nu_z\nu_x\tilde{X}_2(\underline{\nu}) \\
-\nu_x\nu_y\tilde{X}_3(\underline{\nu}) & \nu_z^2\tilde{X}_1(\underline{\nu}) + \nu_x^2\tilde{X}_3(\underline{\nu}) & -\nu_z\nu_y\tilde{X}_1(\underline{\nu}) \\
-\nu_x\nu_z\tilde{X}_2(\underline{\nu}) & -\nu_y\nu_z\tilde{X}_1(\underline{\nu}) & \nu_x^2\tilde{X}_2(\underline{\nu}) + \nu_y^2\tilde{X}_1(\underline{\nu})
\end{bmatrix} \\
\tilde{T}_\Phi^I(\underline{\nu}) &= 2\pi i \begin{bmatrix}
2\nu_x\tilde{\Phi}_1(\underline{\nu}) & \nu_y\tilde{\Phi}_1(\underline{\nu}) + \nu_x\tilde{\Phi}_2(\underline{\nu}) & \nu_z\tilde{\Phi}_1(\underline{\nu}) + \nu_x\tilde{\Phi}_3(\underline{\nu}) \\
\nu_y\tilde{\Phi}_1(\underline{\nu}) + \nu_x\tilde{\Phi}_2(\underline{\nu}) & 2\nu_y\tilde{\Phi}_2(\underline{\nu}) & \nu_z\tilde{\Phi}_2(\underline{\nu}) + \nu_y\tilde{\Phi}_3(\underline{\nu}) \\
\nu_z\tilde{\Phi}_1(\underline{\nu}) + \nu_x\tilde{\Phi}_3(\underline{\nu}) & \nu_z\tilde{\Phi}_2(\underline{\nu}) + \nu_y\tilde{\Phi}_3(\underline{\nu}) & 2\nu_z\tilde{\Phi}_3(\underline{\nu})
\end{bmatrix}
\end{aligned} \qquad (13)$$

we change (18) - (20) to:

$$\begin{aligned}\tilde{P}_x\left(\nu_x,\nu_y,\nu_z\right) &= \left(\nu_y/\cos\theta\right)^2\tilde{X}_1\left(\nu_x,\nu_y,\nu_z\right)\\ &+ \left(\nu_x\cos\theta\right)^2\tilde{X}_2\left(\nu_x,\nu_y,\nu_z\right)\\ &+ \left(\nu_x\sin\theta\right)^2\tilde{X}_3\left(\nu_x,\nu_y,\nu_z\right), \qquad (22)\\ \tilde{P}_y\left(\nu_x,\nu_y,\nu_z\right) &= \left(\nu_y\cos\theta\right)^2\tilde{X}_1\left(\nu_x,\nu_y,\nu_z\right)\\ &+ \left(\nu_z/\sin\theta\right)^2\tilde{X}_2\left(\nu_x,\nu_y,\nu_z\right)\\ &+ \left(\nu_y\sin\theta\right)^2\tilde{X}_3\left(\nu_x,\nu_y,\nu_z\right), \qquad (23)\\ \tilde{P}_z\left(\nu_x,\nu_y,\nu_z\right) &= \left(\nu_z\sin\phi\right)^2\tilde{X}_1\left(\nu_x,\nu_y,\nu_z\right)\\ &+ \left(\nu_z\cos\phi\right)^2\tilde{X}_2\left(\nu_x,\nu_y,\nu_z\right)\\ &+ \left(\nu_x/\sin\phi\right)^2\tilde{X}_3\left(\nu_x,\nu_y,\nu_z\right). \qquad (24)\end{aligned}$$

Notice that ν_{v_1}, ν_{v_2} and ν_{u_3} each has two expressions, $\nu_{v_1} = -\nu_y/\cos\theta = \nu_z/\sin\theta$, $\nu_{v_2} = -\nu_x/\cos\theta = \nu_z/\sin\theta$, $\nu_{u_3} = -\nu_x/\sin\phi = \nu_y/\cos\phi$.

Using Cramer's rule [48], the solutions of $\tilde{X}_1$, $\tilde{X}_2$ and $\tilde{X}_3$ to the system of linear equations are:

$$\begin{aligned}\tilde{X}_1 &= \frac{(b_2c_3-b_3c_2)\tilde{P}_x+(b_3c_1-b_1c_3)\tilde{P}_y+(b_1c_2-b_2c_1)\tilde{P}_z}{a_3b_1c_2+a_2b_3c_1+a_1b_2c_3-a_2b_1c_3-a_3b_2c_1-a_1b_3c_2},\\ \tilde{X}_2 &= \frac{(a_3c_2-a_2c_3)\tilde{P}_x+(a_1c_3-a_3c_1)\tilde{P}_y+(a_2c_1-a_1c_2)\tilde{P}_z}{a_3b_1c_2+a_2b_3c_1+a_1b_2c_3-a_2b_1c_3-a_3b_2c_1-a_1b_3c_2},\\ \tilde{X}_3 &= \frac{(a_2b_3-a_3b_2)\tilde{P}_x+(a_3b_1-a_1b_3)\tilde{P}_y+(a_1b_2-a_2b_1)\tilde{P}_z}{a_3b_1c_2+a_2b_3c_1+a_1b_2c_3-a_2b_1c_3-a_3b_2c_1-a_1b_3c_2},\end{aligned} \qquad (25)$$

where

$$\begin{aligned}a_1 &= (\nu_y/\cos\theta)^2 = (\nu_z/\sin\theta)^2, \quad b_1 = (\nu_x\cos\theta)^2,\\ c_1 &= (\nu_x\sin\theta)^2,\\ a_2 &= (\nu_y\cos\theta)^2, \quad b_2 = (\nu_z/\sin\theta)^2 = (\nu_x/\cos\theta)^2,\\ c_2 &= (\nu_y\sin\theta)^2,\\ a_3 &= (\nu_z\sin\phi)^2, \quad b_3 = (\nu_z\cos\phi)^2,\\ c_3 &= (\nu_x/\sin\phi)^2 = (\nu_y/\cos\phi)^2.\end{aligned}$$

Once solving for $\tilde{X}_1$, $\tilde{X}_2$ and $\tilde{X}_3$, we can evaluate X_1, X_2, X_3 via the inverse Fourier transform. However, interpolating from polar to Cartesian coordinates in direct Fourier reconstruction produces angular aliasing artifacts in the reconstructed image [49]. Hence, we reconstruct X_1, X_2, X_3 slice by slice as in CT with a filtered back-projection method using an external Hamming window. Using a filtered back-projection reconstruction by filtering in frequency space or providing a convolution reconstruction in real space also suppresses high frequency noise providing smoother results.

Taking X_1 as an example. It can be denoted as the 3D inverse Fourier transform as

$$X_1(x,y,z) = \int_0^\infty\int_0^\infty\int_0^\infty \tilde{X}_1\left(\nu_x,\nu_y,\nu_z\right)e^{2\pi i\left(x\nu_x+y\nu_y+z\nu_z\right)}d\nu_x d\nu_y d\nu_z. \qquad (26)$$

If we transform the coordinates according to $[\nu_x,\nu_y,\nu_z]^T = [-\nu_u,-\nu_v\cos\theta,\nu_v\sin\theta]^T$, (26) becomes

$$\begin{aligned}&X_1(x,y,z)\\ &= \int_0^{2\pi}\int_0^\infty\int_0^\infty \tilde{X}_1(\nu_u,\nu_v,\theta)e^{2\pi i(-x\nu_u-y\nu_v\cos\theta+z\nu_v\sin\theta)}\\ &\quad\times\nu_v d\nu_u d\nu_v d\theta,\\ &= \int_0^{\pi}\int_{-\infty}^\infty\int_{-\infty}^\infty \tilde{X}_1(\nu_u,\nu_v,\theta)e^{2\pi i(-x\nu_u-y\nu_v\cos\theta+z\nu_v\sin\theta)}\,|\nu_v|\\ &\quad\times d\nu_u d\nu_v d\theta. \qquad (27)\end{aligned}$$

With the same coordinate transformation, the expression of $\tilde{X}_1$ in (25) becomes

$$\begin{aligned}&\tilde{X}_1(\nu_u,\nu_v,\theta)\\ &= \frac{-(\nu_v)^2\tilde{P}_x+(\nu_u\cos\theta)^2\tilde{P}_y+\left((\sin\theta)^2\nu_v\right)^2\left(1+(\cos\theta)^2\right)\tilde{P}_z}{\left((\cos\theta)^3\nu_u\nu_v\right)^2+(\nu_v\sin\theta)^4-(\nu_v\sin\theta\cos\theta)^4-(\nu_v)^4}.\end{aligned} \qquad (28)$$

Substituting this expression into (27) for $\tilde{X}_1$, we obtain in (29), as shown at the bottom of the next page.

The first integral is the same as the back-projection in a classic filtered back-projection (FBP) algorithm. The inner double integral can be seen as the inverse Fourier transform of the sum of three terms is obtained in (30), as shown at the bottom of the next page. Here each term is the projection along one axis filtered by the product of the characteristic ramp filter $|\nu_v|$ and a factor of coordinate transformation.

We denote the inverse Fourier transform of the above three terms as M_x, M_y and M_z, and rewrite (29) as

$$\begin{aligned}X_1(x,y,z) = \int_0^\pi [&\mathrm{M}_x(-x,-y\cos\theta+z\sin\theta,\theta)\\ &+\mathrm{M}_y(-x,-y\cos\theta+z\sin\theta,\theta)\\ &+\mathrm{M}_z(-x,-y\cos\theta+z\sin\theta,\theta)]d\theta.\end{aligned} \qquad (31)$$

This is the back-projection of the filtered projections M_x, M_y and M_z. Similar expressions can be derived for X_2 and X_3. Then the solenoidal component is calculated according to (9). However, to avoid the differentiation in computing the solenoidal components in (9), we use the differentiation property of Fourier transform in (30). For example, instead of implementing $\partial^2X_1/\partial z^2$ after X_1 is ready, we multiply terms in (30) with $-\nu_z^2\tilde{X}_1$ and then back-project the sum to directly obtain the result.

The algorithm to reconstruct the solenoidal component of the tensor field is summarized below as Reconstruction 1. In the implementation, we simulate $p\frac{\theta\theta}{\theta}$ around x, y, z axes to obtain projections P_x, P_y, P_z. Then $\tilde{P}_x\left(\nu_{u_1},\nu_{v_1}\right)$, $\tilde{P}_y\left(\nu_{u_2},\nu_{v_2}\right)$, and $\tilde{P}_z\left(\nu_{u_3},\nu_{v_3}\right)$ are calculated via the 2D Fourier transform of these projections. We transform the coordinate system according to (21) to keep projections around three axes sampled in the same grid. After that, $X_1(x,y,z)$ can be calculated by filtering the projections as in (30) and then back-projecting the filtered projections as in (31).

Reconstruction 1 Solenoidal Component From $p_{\underline{\theta}}^{\theta\theta}$

Input: Directional X-ray Projections P_x, P_y, P_z
for m = x, y, z **do**
Compute $\tilde{\mathrm{P}}_m$: 2D Fourier transform of P_m and interpolation according to (21)
Compute $\tilde{\mathrm{M}}_m$: Filter $\tilde{\mathrm{P}}_m$ according to (30)
Compute M_m: Inverse Fourier transform of $\tilde{\mathrm{M}}_m$
end for
X_1 = Back-project $\mathrm{M}_x, \mathrm{M}_y$ and M_z, according to (31)
Similarly obtain X_2 and X_3
Output: the solenoidal component according to (9)

B. Irrotational Component Reconstruction Using $p_{\underline{\theta}}^{\beta\beta}$

To reconstruct the irrotational component, we use Q_x, Q_y, Q_z to identify projections $p_{\underline{\theta}}^{\beta\beta}$ acquired rotating about x, y and z axes and reconstruct the three unknowns Φ_1, Φ_2 and Φ_3.

For projections acquired around the x-axis, ϕ in (3) is 90°, thus summing (16) and (17):

$$\begin{aligned}&\tilde{Q}_x\left(\nu_{u_1},\nu_{v_1}\right)\\&=\left(\nu_{u_1}\sin\theta\right)^2\tilde{X}_2\left(\nu_{u_1}\underline{\alpha}_1+\nu_{v_1}\underline{\beta}_1\right)+\left(\nu_{u_1}\cos\theta\right)^2\\&\quad\times\tilde{X}_3\left(\nu_{u_1}\underline{\alpha}_1+\nu_{v_1}\underline{\beta}_1\right)-2\nu_{v_1}\cos\theta\tilde{\Phi}_2\left(\nu_{u_1}\underline{\alpha}_1+\nu_{v_1}\underline{\beta}_1\right)\\&\quad+2\nu_{v_1}\sin\theta\tilde{\Phi}_3\left(\nu_{u_1}\underline{\alpha}_1+\nu_{v_1}\underline{\beta}_1\right).\end{aligned}\tag{32}$$

For projections acquired around the y-axis, ϕ equals 0° in (3), thus:

$$\begin{aligned}\tilde{Q}_y\left(\nu_{u_2},\nu_{v_2}\right)&=\left(\nu_{u_2}\sin\theta\right)^2\tilde{X}_1\left(\nu_{u_2}\underline{\alpha}_2+\nu_{v_2}\underline{\beta}_2\right)\\&\quad+\left(\nu_{u_2}\cos\theta\right)^2\tilde{X}_3\left(\nu_{u_2}\underline{\alpha}_2+\nu_{v_2}\underline{\beta}_2\right)\\&\quad-2\nu_{v_2}\cos\theta\tilde{\Phi}_1\left(\nu_{u_2}\underline{\alpha}_2+\nu_{v_2}\underline{\beta}_2\right)\\&\quad+2\nu_{v_2}\sin\theta\tilde{\Phi}_3\left(\nu_{u_2}\underline{\alpha}_2+\nu_{v_2}\underline{\beta}_2\right).\end{aligned}\tag{33}$$

For projections acquired around the z-axis, θ is 90° in (3), hence:

$$\begin{aligned}\tilde{Q}_z\left(\nu_{u_3},\nu_{v_3}\right)&=\left(\nu_{u_3}\cos\phi\right)^2\tilde{X}_1\left(\nu_{u_3}\underline{\alpha}_3+\nu_{v_3}\underline{\beta}_3\right)\\&\quad+\left(\nu_{u_3}\sin\phi\right)^2\tilde{X}_2\left(\nu_{u_3}\underline{\alpha}_3+\nu_{v_3}\underline{\beta}_3\right)\\&\quad+2\nu_{v_3}\tilde{\Phi}_3\left(\nu_{u_3}\underline{\alpha}_3+\nu_{v_3}\underline{\beta}_3\right).\end{aligned}\tag{34}$$

In these three equations, $\tilde{X}_1$, $\tilde{X}_2$ and $\tilde{X}_3$ have been calculated as discussed in Section *A*. We then subtract terms of $\tilde{X}_1$, $\tilde{X}_2$ and $\tilde{X}_3$ from $\tilde{Q}_x$, $\tilde{Q}_y$ and $\tilde{Q}_z$ in (32)-(34) to form the following expressions $\tilde{N}_x$, $\tilde{N}_y$ and $\tilde{N}_z$ in terms of the three unknowns Φ_1, Φ_2 and Φ_3:

$$\begin{aligned}&\tilde{N}_x\left(\nu_{u_1},\nu_{v_1}\right)\\&=\tilde{Q}_x\left(\nu_{u_1},\nu_{v_1}\right)-\left(\nu_{u_1}\sin\theta\right)^2\tilde{X}_2\left(\nu_{u_1}\underline{\alpha}_1+\nu_{v_1}\underline{\beta}_1\right)\\&\quad-\left(\nu_{u_1}\cos\theta\right)^2\tilde{X}_3\left(\nu_{u_1}\underline{\alpha}_1+\nu_{v_1}\underline{\beta}_1\right),\\&=-2\nu_{v_1}\cos\theta\tilde{\Phi}_2\left(\nu_{u_1}\underline{\alpha}_1+\nu_{v_1}\underline{\beta}_1\right)\\&\quad+2\nu_{v_1}\sin\theta\tilde{\Phi}_3\left(\nu_{u_1}\underline{\alpha}_1+\nu_{v_1}\underline{\beta}_1\right),\end{aligned}\tag{35}$$

$$\begin{aligned}&\tilde{N}_y\left(\nu_{u_2},\nu_{v_2}\right)\\&=\tilde{Q}_y\left(\nu_{u_2},\nu_{v_2}\right)-\left(\nu_{u_2}\sin\theta\right)^2\tilde{X}_1\left(\nu_{u_2}\underline{\alpha}_2+\nu_{v_2}\underline{\beta}_2\right)\\&\quad-\left(\nu_{u_2}\cos\theta\right)^2\tilde{X}_3\left(\nu_{u_2}\underline{\alpha}_2+\nu_{v_2}\underline{\beta}_2\right),\\&=-2\nu_{v_2}\cos\theta\tilde{\Phi}_1\left(\nu_{u_2}\underline{\alpha}_2+\nu_{v_2}\underline{\beta}_2\right)\\&\quad+2\nu_{v_2}\sin\theta\tilde{\Phi}_3\left(\nu_{u_2}\underline{\alpha}_2+\nu_{v_2}\underline{\beta}_2\right),\end{aligned}\tag{36}$$

$$\begin{aligned}&\tilde{N}_z\left(\nu_{u_3},\nu_{v_3}\right)\\&=\tilde{Q}_z\left(\nu_{u_3},\nu_{v_3}\right)-\left(\nu_{u_3}\cos\phi\right)^2\tilde{X}_1\left(\nu_{u_3}\underline{\alpha}_3+\nu_{v_3}\underline{\beta}_3\right)\\&\quad-\left(\nu_{u_3}\sin\phi\right)^2\tilde{X}_2\left(\nu_{u_3}\underline{\alpha}_3+\nu_{v_3}\underline{\beta}_3\right),\\&=2\nu_{v_3}\tilde{\Phi}_3\left(\nu_{u_3}\underline{\alpha}_3+\nu_{v_3}\underline{\beta}_3\right).\end{aligned}\tag{37}$$

Likewise, to solve (35)-(37) for Φ_1, Φ_2 and Φ_3, we change to the global coordinate system $\left(\nu_x,\nu_y,\nu_z\right)$:

$$\tilde{N}_x\left(\nu_x,\nu_y,\nu_z\right)=2\nu_y\tilde{\Phi}_2\left(\nu_x,\nu_y,\nu_z\right)+2\nu_z\tilde{\Phi}_3\left(\nu_x,\nu_y,\nu_z\right)\tag{38}$$

$$\tilde{N}_y\left(\nu_x,\nu_y,\nu_z\right)=2\nu_x\tilde{\Phi}_1\left(\nu_x,\nu_y,\nu_z\right)+2\nu_z\tilde{\Phi}_3\left(\nu_x,\nu_y,\nu_z\right)\tag{39}$$

$$\tilde{N}_z\left(\nu_x,\nu_y,\nu_z\right)=2\nu_z\tilde{\Phi}_3\left(\nu_x,\nu_y,\nu_z\right)\tag{40}$$

$$\begin{aligned}X_1(x,y,z)=&\int_0^{\pi}\int_{-\infty}^{\infty}\int_{-\infty}^{\infty}\frac{-(\nu_v)^2\tilde{P}_x+(\cos\theta\nu_u)^2\tilde{P}_y+\left((\sin\theta)^2\nu_v\right)^2\left(1+(\cos\theta)^2\right)\tilde{P}_z}{\left((\cos\theta)^3\nu_u\nu_v\right)^2+(\sin\theta\nu_v)^4-(\sin\theta\cos\theta\nu_v)^4-(\nu_v)^4}\\&\times e^{2\pi i(-x\nu_u-y\nu_v\cos\theta+z\nu_v\sin\theta)}\left|\nu_v\right|d\nu_u d\nu_v d\theta\end{aligned}\tag{29}$$

$$\begin{aligned}\tilde{\mathrm{M}}_x(\nu_u,\nu_v,\theta)&=\frac{-(\nu_v)^2\tilde{P}_x(\nu_u,\nu_v,\theta)}{\left((\cos\theta)^3\nu_u\nu_v\right)^2+(\sin\theta\nu_v)^4-(\sin\theta\cos\theta\nu_v)^4-(\nu_v)^4}\left|\nu_v\right|\\\tilde{\mathrm{M}}_y(\nu_u,\nu_v,\theta)&=\frac{(cos\theta\nu_u)^2\tilde{P}_y(\nu_u,\nu_v,\theta)}{\left((\cos\theta)^3\nu_u\nu_v\right)^2+(\sin\theta\nu_v)^4-(\sin\theta\cos\theta\nu_v)^4-(\nu_v)^4}\left|\nu_v\right|\\\tilde{\mathrm{M}}_z(\nu_u,\nu_v,\theta)&=\frac{\left((sin\theta)^2\nu_v\right)^2\left(1+(cos\theta)^2\right)\tilde{P}_z(\nu_u,\nu_v,\theta)}{\left((\cos\theta)^3\nu_u\nu_v\right)^2+(\sin\theta\nu_v)^4-(\sin\theta\cos\theta\nu_v)^4-(\nu_v)^4}\left|\nu_v\right|\end{aligned}\tag{30}$$

After coordinate system transformation, the solutions of $\tilde{\Phi}_1$, $\tilde{\Phi}_2$ and $\tilde{\Phi}_3$ are:

$$\tilde{\Phi}_1 = \frac{\tilde{N}_y - \tilde{N}_z}{2v_x}$$
$$\tilde{\Phi}_2 = \frac{\tilde{N}_x - \tilde{N}_z}{2v_y}$$
$$\tilde{\Phi}_3 = \frac{\tilde{N}_z}{2v_z} \tag{41}$$

Like the reconstruction of X_1, we reconstruct Φ_1 with projections around the x-axis. Exchanging v_x, v_y and v_z to v_u, v_v in (41), we have

$$\tilde{\Phi}_1 = \frac{\tilde{N}_y - \tilde{N}_z}{-2v_u}. \tag{42}$$

The 3D inverse Fourier transform of $\tilde{\Phi}_1$ is

$$\Phi_1(x, y, z) = \int_0^\infty \int_0^\infty \int_0^\infty \tilde{\Phi}_1(v_x, v_y, v_z) e^{2\pi i(xv_x + yv_y + zv_z)} dv_x dv_y dv_z. \tag{43}$$

We transform v_x, v_y and v_z to v_u and v_v:

$$\Phi_1(x, y, z) = \int_0^{2\pi} \int_0^\infty \int_0^\infty \tilde{\Phi}_1(v_u, v_v, \theta) e^{2\pi i(-xv_u - yv_v\cos\theta + zv_v\sin\theta)} \times v_v dv_u dv_v d\theta.$$

Substituting the expression for $\tilde{\Phi}_1$:

$$\Phi_1(x, y, z) = -\int_0^{2\pi} \int_0^\infty \int_0^\infty \frac{\tilde{N}_y - \tilde{N}_z}{2v_u} e^{2\pi i(-xv_u - yv_v\cos\theta + zv_v\sin\theta)} v_v dv_u dv_v d\theta$$
$$= -\int_0^{\pi} \int_{-\infty}^\infty \int_{-\infty}^\infty \frac{\tilde{N}_y - \tilde{N}_z}{2|v_u|} e^{2\pi i(-xv_u - yv_v\cos\theta + zv_v\sin\theta)} |v_v| \times dv_u dv_v d\theta. \tag{44}$$

Let

$$\tilde{L}_y = \frac{\tilde{N}_y}{2|v_u|} |v_v|,$$
$$\tilde{L}_z = \frac{\tilde{N}_z}{2|v_u|} |v_v|, \tag{45}$$

then taking the inverse Fourier transform, we have $\Phi_1(x, y, z)$ obtained by the back-projection of L_y and L_z:

$$\Phi_1(x, y, z) = \int_0^\pi [L_y(-x, -ycos\theta + zsin\theta, \theta) - L_z(-x, -ycos\theta + zsin\theta, \theta)] d\theta. \tag{46}$$

Φ_2 and Φ_3 can be derived similarly.

The algorithm to reconstruct the irrotational component of the tensor field is presented below as Reconstruction 2. We also implement a hamming window in the filtered back-projection method based on the expressions for Φ_1, Φ_2 and Φ_3. The implementation to reconstruct the irrotational component is the same as that for solenoidal component presented in Reconstruction 1.

Reconstruction 2 Irrotational Component From $p_{\underline{\theta}}^{\underline{\beta}\,\beta}$

Input: Directional X-ray Projections Q_x, Q_y, Q_z
for m = x, y, z **do**
  Compute $\tilde{Q}_m$: 2D Fourier transform of Q_m
  Compute $\tilde{N}_m$: Subtract $\tilde{Q}_m$ according to (35)-(37) and interpolate according to (21)
  Compute $\tilde{L}_m$: Filter $\tilde{N}_m$
  Compute L_m: Inverse Fourier transform of $\tilde{L}_m$
end for
Reconstruct Φ_1: Back-projection according to (46)
Similarly obtain Φ_2 and Φ_3
Output: the irrotational component according to (12)

IV. Implementation

The following presents how we implemented the simulation study to assess our algorithm. In particular we used two phantoms, one a discrete numerical phantom and the other a realistic diffusion tensor field of an excised human heart.

A. Discrete Representation of the Tensor Field

The discretized tensor field was stored as a $9 \times N^3$ matrix, containing the nine elements of the second rank tensor field for each voxel of an $N \times N \times N$ voxel grid. Projection data were represented by a $3 \times n_\theta \times h \times w$ matrix, where for each of the 3 rotation axes (X, Y and Z axes), $h \times w$ tomographic projections were acquired at n_θ angular steps with h being the number of two-dimensional slices and w being the radius of rotation.

B. Phantoms

1) A Simple Illustrative Phantom: The first phantom was constructed using (9) and (12) from two balls of uniform intensities placed in a $128 \times 128 \times 128$ array as shown in Fig. 2(a). Six $128 \times 128 \times 128$ arrays were assembled, such that in each array the two balls took on one of the scalar values for X_1, X_2, X_3, Φ_1, Φ_2 and Φ_3 in Fig. 2(b). Thus, each array had two balls with the same constant value and a uniform background. Using first and second order partial derivatives as shown in (9) and (12), solenoidal and irrotational components were generated separately, and then summed to obtain the tensor field for the phantom. The generated solenoidal, irrotational components and tensor field only contain the borders of the balls, the other space is 0. Fig. 3 (a), (b), (c) display the x-y slice through the center of the 9 elements for the solenoidal component, the irrotational component, and the sum forming the tensor field for the phantom, respectively.

2) Cardiac Diffusion Tensor Image: The second phantom used for the simulations in this work was a cardiac diffusion tensor image that was obtained by scanning a normal excised human heart with a 4-element phased array coil on a 1.5 T

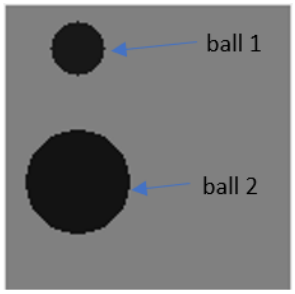

(a)

	ball 1	ball 2	background
X_1	19	15	100
X_2	12	32	130
X_3	10.3	10	113
Φ_1	6.9	19	31
Φ_2	15	15	44
Φ_3	16	26	53

(b)

Fig. 2. Six scalar fields were used to form the tensor field using (9) and (12). (a) Illustration of the central transaxial slice through the two balls that were assigned the scalar values in the table (b) for the tensor potential (X_1, X_2, X_3) and the vector potential (Φ_1, Φ_2, Φ_3).

GE CV/I MRI Scanner (GE Medical System, Waukesha, WI). Details about the heart and acquisition parameters are described in [50].

The diffusion tensor T was obtained from [50] as eigenvectors $\underline{\varepsilon}_1$, $\underline{\varepsilon}_2$ and $\underline{\varepsilon}_3$ with eigenvalues λ_1, λ_2 and λ_3 for $\lambda_1 \geq \lambda_2 \geq \lambda_3 \geq 0$. The data set was arranged in a 256 $\times$ 256 $\times$ 134 array for each eigenvector and eigenvalue, with a voxel size of 429.7 μm $\times$ 429.7 μm $\times$1000 μm. Denoting V as the matrix of eigenvectors and $D = diag\ (\lambda_1, \lambda_2, \lambda_3)$ as the diagonal matrix of eigenvalues, the diffusion tensor was computed from $T = VDV^T$. The 9 elements of the cardiac diffusion tensor phantom are shown in Fig. 4, which were reformulated from the eigenvalues and eigenvectors.

C. Forward Model

We used the same method to generate the projections for the simple numerical phantom and the heart diffusion tensor field calculated using the eigenvectors and eigenvalues. Both the phantom and projections had the same pixel size. A discrete version of the scalar projections $p_{\underline{\theta}}^{\underline{\theta}\,\underline{\theta}}$ and $p_{\underline{\theta}}^{\underline{\beta}\,\underline{\beta}}$ were formed using ray tracing. For example, taking $p_{\underline{\theta}}^{\underline{\theta}\,\underline{\theta}}$ acquired around the x-axis, ϕ in (3) is 90° and $\underline{\theta} = (0, sin\theta, cos\theta)$. Due to symmetry, t_{yz} is the same as t_{zy}. Our approach generated each projection one angle (one θ value in this example) at a time for the directional X-ray transform

$$p_{\underline{\theta}}^{\underline{\theta}\,\underline{\theta}} = \int_{-\infty}^{\infty} \underline{\theta}^T T\left(t\underline{\theta} + u\underline{\alpha} + v\underline{\beta}\right)\underline{\theta} dt$$
$$= \int_{-\infty}^{\infty} \left(t_{yy} sin^2\theta + 2t_{yz} sin\theta cos\theta + t_{zz} cos^2\theta\right) dt.$$

Using ray-tracing, the contribution of each voxel to the integral was calculated by multiplying the length of the voxel intersection with the ray multiplied by the value of the tensor elements (t_{yy}, t_{yz} and t_{zz}) times their coefficients ($sin^2\theta$, $2sin\theta cos\theta$ and $cos^2\theta$) in the voxel. For each of the three rotation axes, the phantom rotated through 180° in 1° increments so that a total of 540 parallel projections were formed about three axes.

D. Evaluation

To evaluate the difference between the reconstruction results and the phantom, we used the relative 2-norm error by summing the normalized difference between the reconstruction and the true value for each tensor element and for each first principal eigenvalue, as in (47) and (48), shown at the bottom of the next page. Here the difference is calculated for each voxel i and normalized by the difference between the maximum true value and the minimum true value in the N voxels of the region of interest (ROI).

Fractional anisotropy (FA) was also used to deduce the accuracy of the reconstructions. FA gives the degree of anisotropy of a diffusion process and is defined using the eigenvalues (λ_1, λ_2 and λ_3) of the tensor:

$$\mathrm{FA} = \sqrt{\frac{3}{2}} \frac{\sqrt{(\lambda_1 - \lambda)^2 + (\lambda_2 - \lambda)^2 + (\lambda_3 - \lambda)^2}}{\sqrt{\lambda_1^2 + \lambda_2^2 + \lambda_3^2}} \tag{49}$$

where $\lambda = \frac{\lambda_1 + \lambda_2 + \lambda_3}{3}$.

To evaluate the noise property of the algorithm, we calculated the signal-to-noise ratio (SNR) for the first principal eigenvalue of the reconstructions, which is defined:

$$SNR = \frac{mean(\lambda_1)}{\sigma_{\lambda_1}} \tag{50}$$

where $mean\,(\lambda_1)$ and σ_{λ_1} are the mean and the standard deviation of the reconstructed tensor principal eigenvalue λ_1 in the ROI, respectively.

V. Results

A. A Simple Illustrative Phantom

1) Solenoidal Component: Both the qualitative and quantitative results show that the algorithm is accurate in reconstructing the solenoidal component of the simulated tensor field for the simple illustrative phantom. We reconstructed the solenoidal component according to Reconstruction I. The reconstructed image matrix was 128 $\times$ 128 $\times$ 128, the same as that of the phantom. Fig. 5 shows the central slice, where the three columns from left to right form the nine elements of the phantom (as defined in Fig. 3(a)), the reconstructed image, and their profiles along the red line in the first column in Fig. 5(a). The profiles of the reconstructed image match those of the phantom.

Table I summarizes for each tensor element the results of the errors calculated according to (47). The errors are small (<0.0008). Due to symmetry of the tensor, T_{xy} and T_{yx} are identical, so are T_{xz} and T_{zx}; and T_{yz} and T_{zy}.

2) Irrotational Component: Fig. 6 presents each element of the estimates through the center slice of the irrotational component for the simulated phantom. The projections $p_{\underline{\theta}}^{\underline{\beta}\,\underline{\beta}}$ acquired around three axes were reconstructed following the steps in Reconstruction 2. Profiles in Fig. 6 indicate the similarity between the reconstructed images and the phantom. We calculated the relative error for each reconstructed element of the reconstructions as listed in Table I. The errors are small but mostly larger than those for the solenoidal component.

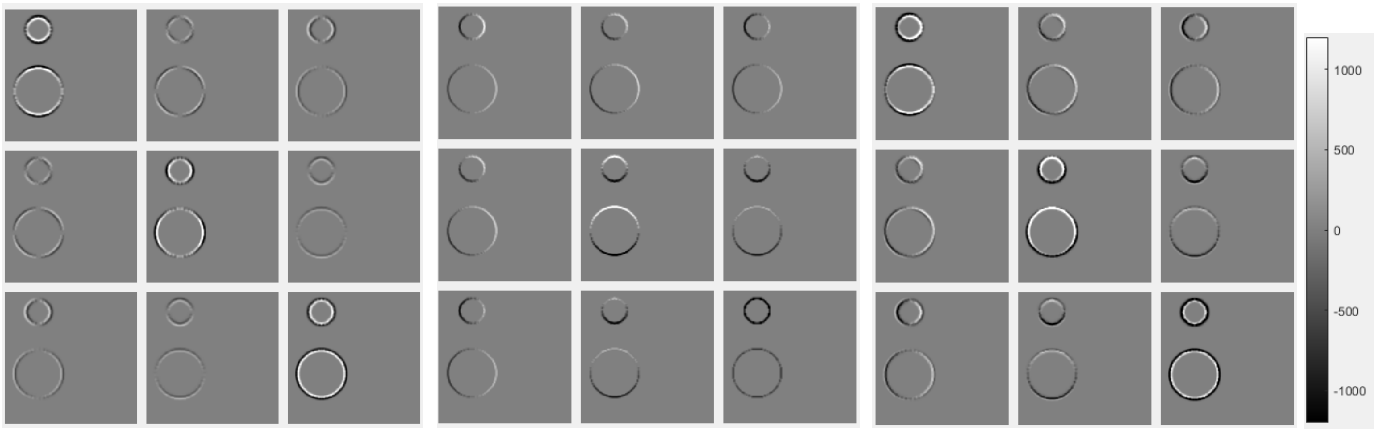

Fig. 3. The x-y slice through the center of the 9 elements for (a) solenoidal component, (b) irrotational component and (c) tensor field.

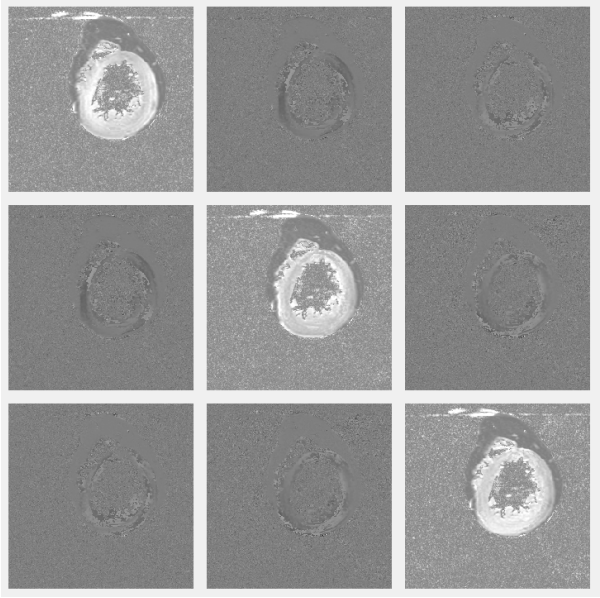

Fig. 4. Nine elements of cardiac diffusion tensor phantom.

TABLE I
THE RELATIVE ERROR CALCULATED ACCORDING TO (47) FOR EACH ELEMENT OF THE SOLENOIDAL COMPONENT, IRROTATIONAL COMPONENT AND TENSOR FIELD FOR THE SIMPLE ILLUSTRATIVE PHANTOM

	solenoidal component	irrotational component	tensor field
T_{xx}	7.4057e-5	2.0640e-4	2.4870e-4
T_{xy}/T_{yx}	3.1368e-4	1.0679e-3	8.5493e-4
T_{xz}/T_{zx}	5.1750e-4	6.9623e-4	6.3424e-4
T_{yy}	8.4666e-5	5.2978e-4	7.2026e-4
T_{yz}/T_{zy}	7.3759e-4	2.2040e-4	2.2134e-3
T_{zz}	3.8806e-4	3.1039e-4	1.5316e-3

3) Tensor Field: The reconstruction of the tensor field is obtained by summing the solenoidal component and the irrotational component. The x-y slice through the center of the 9 elements of the reconstructions together with that of the phantom are given in Fig. 7. Some Gibbs artifacts are in the profiles at the sharp boundaries. The quantitative results in Table I show that the errors for the reconstructed tensor field are small but generally larger than each of its solenoidal and irrotational components, except for T_{xy}/T_{yx} and T_{xz}/T_{zx}.

B. Cardiac Diffusion Tensor Image

The solenoidal and irrotational component of the cardiac diffusion tensor field with image matrix size of 256 × 256 × 256 were estimated from simulated projections with Gaussian noise added. The Gaussian noise was with zero mean and two

$$S_t(T_{uv}) = \frac{\sum_{i=1}^{N}\left(\frac{Recon_{T_{uv}^i} - True_{T_{uv}^i}}{\max\limits_{k=1,\cdots,N}\left(True_{T_{uv}^k}\right) - \min\limits_{k=1,\cdots,N}\left(True_{T_{uv}^k}\right)}\right)^2}{N} \tag{47}$$

$$S_e(E_{11}) = \frac{\sum_{i=1}^{N}\left(\frac{Recon_{E_{11}^i} - True_{E_{11}^i}}{\max\limits_{k=1,\cdots,N}\left(True_{E_{11}^k}\right) - \min\limits_{k=1,\cdots,N}\left(True_{E_{11}^k}\right)}\right)^2}{N} \tag{48}$$

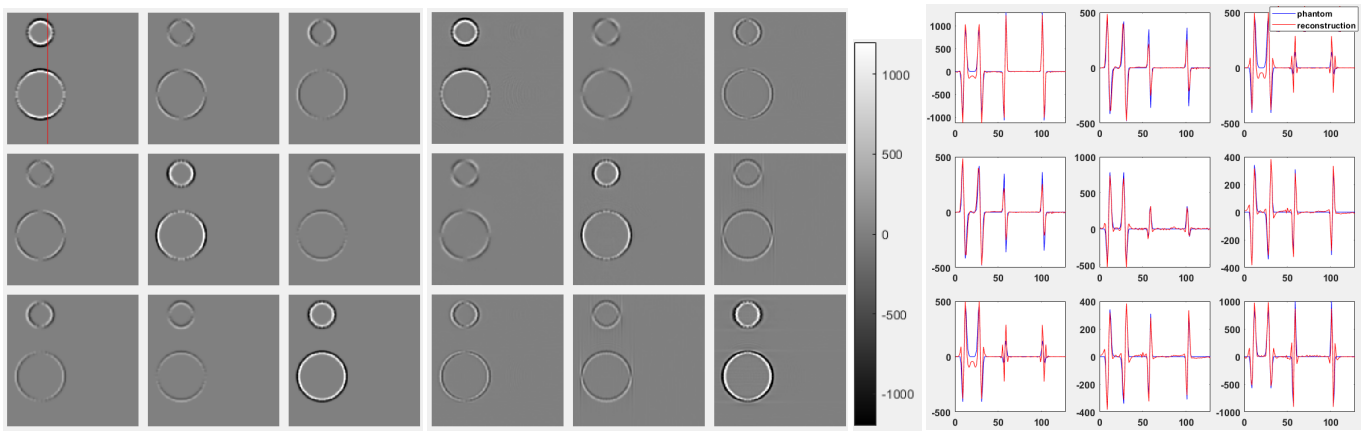

Fig. 5. Reconstruction of the solenoidal component of the phantom. (a) The x-y slice through the center of the 9 elements of the phantom, (b) The x-y slice through the center of the 9 elements of the reconstructed image, (c) Profiles in each element along the red line as example in (a).

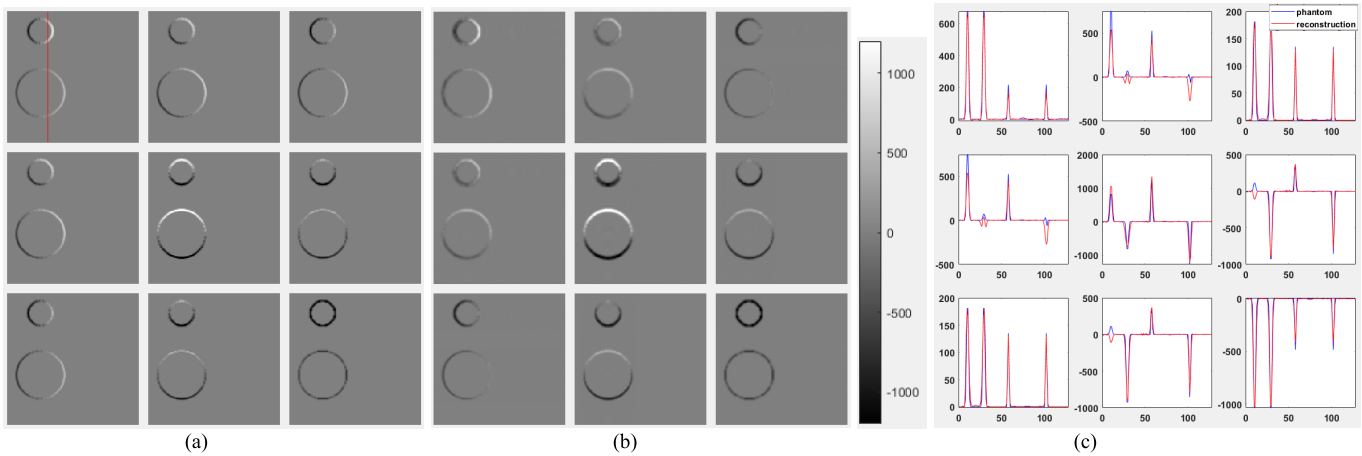

Fig. 6. Reconstruction of the irrotational component of the phantom. (a) The x-y slice through the center of the 9 elements of the phantom, (b) The x-y slice through the center of the 9 elements of the reconstructed image, (c) Profiles in each element along the red line as example in (a).

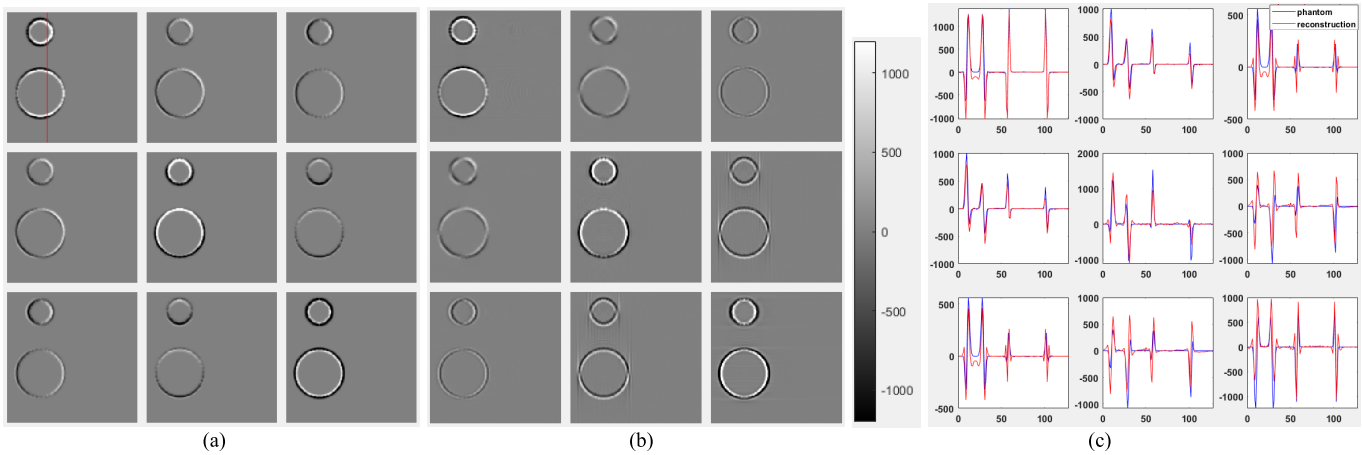

Fig. 7. Reconstruction of the tensor field of the phantom [solenoidal + irrotational]. (a) The x-y slice through the center of the 9 elements of the phantom, (b) The x-y slice through the center of the 9 elements of the reconstructed image, (c) Profiles in each element along the red line as example in (a).

different standard derivations (0.01 and 0.02). Summing the reconstructed solenoidal and irrotational components resulted in the complete tensor field. The reconstructions were then transformed into a matrix formulation of the eigenvalues and eigenvectors.

The first principal eigenvalues for three slices are shown in Fig. 8 and the relative errors are listed in Table II for the first principal eigenvalue calculated according to (48). Fig. 9 gives the FA calculated according to (49) for the same three slices. Also, Table III lists the SNR calculated according to (50).

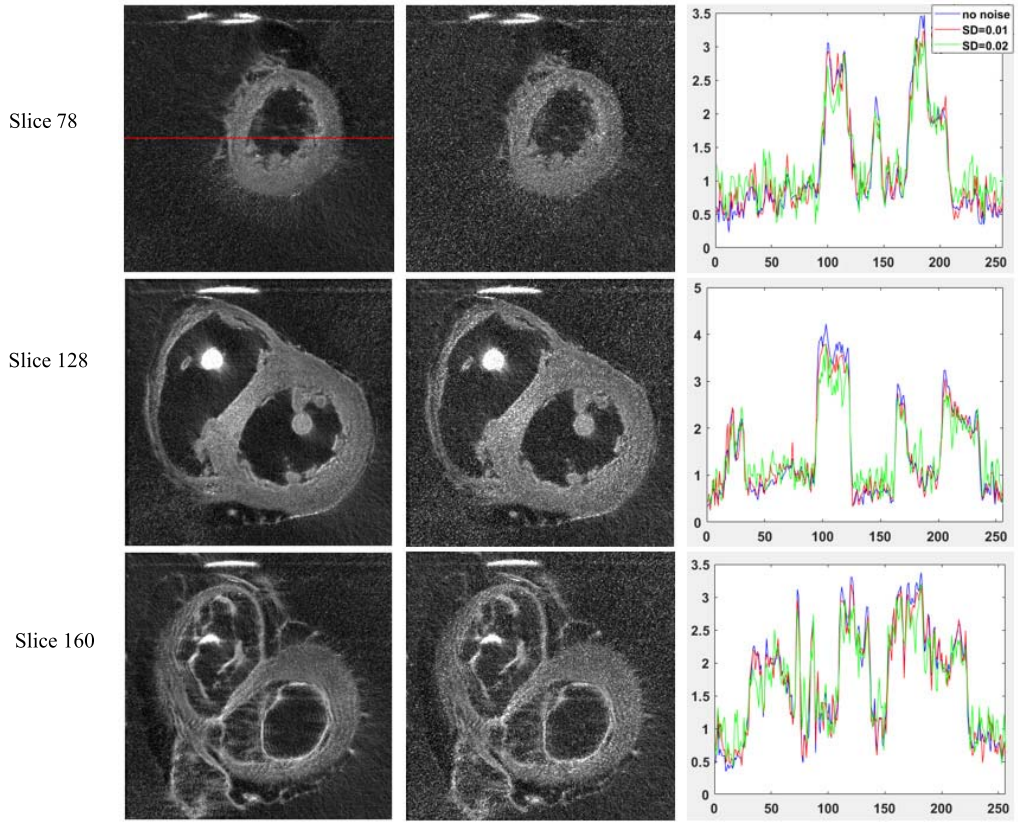

Fig. 8. First principal eigenvalue of reconstructed image with Gaussian noise SD = 0.01 [solenoidal + irrotational] (left); reconstructed image with Gaussian noise SD = 0.02 [solenoidal + irrotational] (middle); and profiles along the red line (right). The series of images from top to bottom are slice 78, slice 128, slice 160, respectively.

TABLE II
THE RELATIVE ERROR FOR FIRST PRINCIPAL EIGENVALUES OF THE CARDIAC DIFFUSION TENSOR PHANTOM, CALCULATED ACCORDING TO (48), FOR DIFFERENT NOISE LEVELS IN THREE SLICES. THE ERROR INCREASES WITH THE NOISE VARIANCE

	No noise	SD=0.01	SD=0.02
Slice 78	0.0017	0.0020	0.0033
Slice 128	0.0017	0.0025	0.0049
Slice 160	0.0026	0.0031	0.0058

TABLE III
THE SNR (AS IN (50)) FOR THE FIRST PRINCIPAL EIGENVALUES OF THE CARDIAC DIFFUSION TENSOR PHANTOM FOR DIFFERENT NOISE LEVELS IN THREE SLICES

	No noise	SD=0.01	SD=0.02
Slice 78	21.86	16.71	10.96
Slice 128	22.95	17.73	13.25
Slice 160	15.09	12.73	8.75

In each slice, we chose a relatively uniform ROI to calculate the SNR, which has a value range from 1.65 to 2.53. We can see more degradation in the image quality with higher noise level.

VI. DISCUSSION

This study provides the derivation of a new filtered back-projection algorithm for the reconstruction of tensor fields from data acquired about three axes. The tensor field is decomposed into solenoidal and irrotational components, both of which have three unknown elements. Fourier projection theorem provides relationships between the Fourier transform of the directional X-ray projections and the Fourier transform of the solenoidal and irrotational components of the tensor field [37]–[40]. In solving for the three unknowns in the solenoidal and irrotational component, new filters are formed involving coefficients of three equations times the characteristic ramp filter [see expressions (30) and (45)]. Different from previous work acquiring projections about at least six [51] or three orthogonal axes [43], our proposed algorithm provides the possibility for using projections about three axes to solve the unknowns of the solenoidal and irrotational component separately. The three axes for acquiring projections $p^{\theta\theta}_{\underline{\theta}}$ for the solenoidal component are the same as the three axes for acquiring projections $p^{\beta\beta}_{\underline{\theta}}$ for the irrotational component. All derived formulas lead to an analytical reconstruction algorithm for a tensor field from projections acquired about three axes.

A. Summary of Results

The proposed algorithm provides estimates of a total of 6 unknowns, 3 for the solenoidal and 3 for the irrotational component of the tensor field. Two phantoms were used to evaluate our algorithm. One was a numerical phantom with no special imaging modality in mind from which we could test our algorithm. Potential values were assigned to the solenoidal and irrotational components. Using the definition of

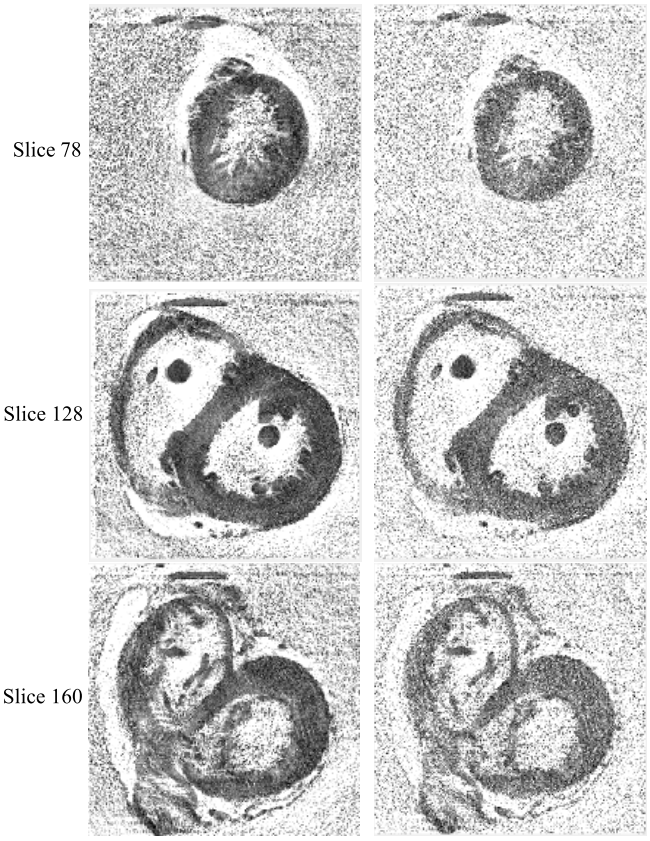

Fig. 9. FA of reconstructed image with Gaussian noise SD = 0.01 (left); reconstructed image with Gaussian noise SD = 0.02 (right). The series of images from top to bottom are slice 78, slice 128, slice 160, respectively.

the curl and gradient in equations (7) and (10), the calculation of the partial derivatives formed tensor elements with two spherical surfaces with interior and background equal to zero. The operations for calculating the gradient and curl were done numerically; thus, the numerical phantom has relatively sharp boundaries but not δ-function singularities on the border of the corresponding spherical shells as one would expect of an analytical reconstructed tensor field. We choose the particular tensor field to evaluate the algorithm performance; in particular, to evaluate the algorithm performance of potential Gibbs artifacts at sharp boundaries. If one wants to interpret the phantom for a particular imaging modality, such as X-ray dark-field imaging, one might construe the phantom to be two spherical surfaces that are imbedded in a uniform background of material with microstructure having anisotropic small-angle scatter at the boundary of the surfaces but virtually no anisotropic small-angle scatter in the background material, only isotropic scatter that attenuates the signal with no anisotropic structure. We see in Fig. 5-7 that the algorithm gives reconstructed results, where at the boundary of the spherical surfaces there are undershoots and overshoots of reconstructed values compared to the original phantom values.

The second phantom was a cardiac diffusion tensor field that was obtained by scanning a normal excised human heart on a 1.5 T GE CV/I MRI Scanner (GE Medical System, Waukesha, WI). Transforming the tensor matrix to its diagonal form provides a singular value decomposition with singular values (eigenvalues), which specify the principal eigenvector with potentially positive and negative elements that one could consider in the first phantom provide the principal direction of the scatter and in the second phantom provide the principal direction of the diffusion relative to the Cartesian coordinate system in Fig. 1. In Fig. 8 the eigenvalues, determined from the reconstructed tensor field of the cardiac diffusion tensor phantom, have larger errors in the reconstruction when noise is added to the projections. These errors are demonstrated better in the FA images in Fig. 9. Our calculations of the signal to noise ratio (SNR) for the first principal eigenvalues (Table III) ranged between 9 and 18, which is low but in line with what one would expect in a single MR-DTI with typical values of 15:1 to 30:1 [52]. It is likely that the noise in the original cardiac tensor image is amplified with the addition of noise in the projections as shown in Table II.

B. X-Ray and Radon Projections of Tensor Fields

Our work in this paper focused on developing a filtered back-projection algorithm for reconstructing longitudinal and transverse X-ray projections, in the same way reconstruction algorithms can be developed for Radon projections of second rank tensor fields [36], [40], [44], [53]–[55]. To illustrate the differences between X-ray and Radon projections, let $\underline{x} = (x, y, z)$ be a point in $\Re^3$ and let the components $t_{ij}(\underline{x})$ of a second rank symmetric tensor field $T(\underline{x})$ be real, rapidly decreasing C^∞ functions defined on $\Re^3$. For the tensor field $T(\underline{x})$, the 3D directional X-ray transform of $T(\underline{x})$ is defined by $p_{\underline{\theta}}^{\underline{a}\,\underline{b}}(\underline{s};\underline{\theta}) = \int_{\Re} \underline{a}^T T(\underline{s}+l\underline{\theta})\underline{b}dl$, and the 3D directional Radon transformation of $T(\underline{x})$ is defined by $r_{\underline{\theta}}^{\underline{a}\,\underline{b}}(t;\underline{\theta}) = \int_{\Re}^{3} \underline{a}^T T(\underline{x})\,\underline{b}\delta(\underline{x}\cdot\underline{\theta}-t)\,d\underline{x}$. These are scalar projection measurements in the direction of $\underline{\theta}$ formed by the product of the tensor T with the three-dimensional unit vectors $\underline{a}$ and $\underline{b}$. For this work we focused primarily on the X-ray scalar projection measurements of the tensor field for vectors $\underline{a}$ and $\underline{b}$ equal to combinations of the orthogonal vectors $\underline{\theta} = (sin\theta cos\phi, sin\theta sin\phi, cos\theta)^T$, $\underline{\alpha} = (-sin\phi, cos\phi, 0)^T$ and $\underline{\beta} = (-cos\theta cos\phi, -cos\theta sin\phi, sin\theta)^T$ in developing a filtered back-projection reconstruction algorithm. In this paper we demonstrate that there is indeed a reconstruction algorithm for transvers reconstruction tomography for a general tensor field using data from only three rotation axes. The method first performs a slice-by-slice reconstruction of six functions by two-dimensional back-projection and filter methods. The components of the tensor field are related to these functions by a linear operator with coefficients that are rational functions of the Fourier transform variables.

C. Solution for Three Orthogonal Axes

It has been shown in other work [42], [55] that three orthogonal chosen directions are sufficient for reconstruction of a tensor field. It has also been shown [33], [34], [36] that three orthogonal axes are sufficient for a full recovery of a vector field from slice-by-slice vector field tomography. In [33] an efficient mollifier methodwas proposed for the three-dimensional vector tomograph problem. The mollifier method

originally proposed by Louis in 1990 [56] is seen throughout his group's work [35], [36], [44] and provides an approximate solution to a continuous inverse problem which one might see very similar to the determination of a regularized solution in the implementation of discrete Bayesian reconstruction methods. For the tensor tomography problem there isthe longitudinal projection in addition to a transverse projection [34], [43] needed for every projection angle to solve for the 6 unknown tensor elements, whereas only one longitudinal projection for each angle is required for the vector tomography problem. For stability it is proposed that 3 orthogonal axes are needed to recover vector fields and 6 orthogonal axes are needed to recover tensor fields [34]. Different from these works, our filtered back-projection algorithm uses longitudinal and transverse projections about three orthogonal axes to solve the unknowns of the solenoidal and irrotational component separately.

D. Helmholtz Decomposition

1) Unbounded Domains: It was shown by Sharafutdinov in [47], that a smooth symmetric tensor field which vanishes rapidly at infinity can be decomposed in a unique way as $t_{ij}(\underline{x}) = t^S_{ij}(\underline{x}) + \frac{1}{2}(\partial_i \varphi_j(\underline{x}) + \partial_j \varphi_i(\underline{x}))$ where $\underline{\varphi}(\underline{x})$ is a vector potential and $T_S(\underline{x})$ is a symmetric solenoidal tensor field, which is divergence free: $\sum_i \partial_i t^S_{ij}(\underline{x}) = \sum_j \partial_j t^S_{ij}(\underline{x}) = 0$. Here we considered a similar decomposition of a symmetric tensor field T: $T(\underline{x}) = T^S_\Psi(\underline{x}) + T^I_\Phi(\underline{x})$, where the symmetric divergent-free solenoidal component $T^S_\Psi(\underline{x})$ is the curl of a tensor potential, $T^S_\Psi(\underline{x}) = \nabla \times \Psi(\underline{x})$, and the symmetric irrotational component $T^I_\Phi(\underline{x})$ is the gradient of a vector potential, $T^I_\Phi(\underline{x}) = \nabla\Phi(\underline{x}) + [\nabla\Phi(\underline{x})]^T$ [37]. This formulation provides a parameterization of the solenoidal and irrotational components each by three scalar functions [(9), (12), and Appendix]. This combines the results of Sharafutdinov [47] with that of the Helmholtz decomposition [57] for vector fields where the solenoidal component is the curl of a vector potential and the irrotational component is the gradient of a scalar potential. We showed in this paper a solution for the solenoidal and irrotational components involves a reconstruction using the Fourier filter back-projection algorithm. Another example o decomposing tensor field into solenoidal and irrotational components to solve for both the tensor elements and potentials is presented in [44]. A solution on general differential manifolds is presented in [41] providing an explicit inverse formula for reconstruction of the solenoidal component of a second rank tensor field from projections acquired about three axes. Different from these decompositions is thesingular value decomposition of a dynamic acquisition of 2-tensors in $\mathbb{R}^2$ ued to solve the inverse of the dynamic tensor projections [58]. This is to our knowledge the first application of tensor tomography to a dynamic acquisition of tensor projections.

2) Bounded Domains: The application of our algorithm to bounded domains is an interesting study. The early work related to vector field tomography on bounded domains resulted in several papers [22], [24], [25], [59]. Specifically, Braun and Hauck [24] recognized that bounded domains admit harmonic vector fields that are both irrotational and solenoidal. Therefore, the decomposition into irrotational and solenoidal components is not unique. In their paper, they proposed that the decomposition should be $V = V^S + V^I + V_H$, where $V^S = \nabla \times \Psi$, $V^I = \nabla\Phi$, and V_H is the harmonic component of the vector field satisfying $\nabla^T V_H = 0$ and $\nabla \times V_H = 0$. The solenoidal component V^S is homogeneous in the sense that the normal component of V^S is zero on the boundary and is totally tangential to the boundary. The curl-free component V^I is homogenous in the sense that the tangential component of V^I vanishes on the boundary and is exactly normal to the boundary. If these Neuman boundary conditions for vector fields are satisfied, then fewer scalar projections are required. A complete summary of work since these early days related to vector tomography can be found in [35]. For tensor tomography Louis *et al.* [36] claimed that the reconstruction on a bounded domain has no unique solution, but claimed the solenoidal part can be uniquely determined because it is overdetermined.Recent work of McGraw *et al.* [60] shows how the decomposition of the tensor field on a bounded domain provides a solenoidal and irrotational component with an addition of a homogeneous component. The generalized Helmholtz decomposition on bounded domain is given by $D_{ij} = \partial_i \phi_j + \varepsilon_{imn}\left(\partial_m \psi_{nj}\right) + H_{ij}$, where the harmonic tensor field, $\left[H_{ij}\right]$, is both solenoidal and irrotational and typically is of small magnitude [60], [61]. The paper by McGraw *et al.* [61] gives some visual examples of the decomposition of tensor fields where it is shown that the harmonic component is a constant background of low intensity.

In our work we took the approach of Sharafutdinov [47] and assumed that the tensor field that we are reconstructing is a sufficiently smooth symmetric tensor field which vanishes rapidly at infinity. We recognize that this may be a stretch if applied to medical images such as the heart where there can be sharp contrast at organ boundaries that may produce background artifacts. Our cardiac diffusion tensor field was obtained from an MR imaging experiment and thus may not have a unique decomposition, whereas the numerical phantom of the two spherical surfaces was designed to have a unique decomposition of the solenoidal and irrotational components by constructing the phantom as the sum of a particular solenoidal and irrotational components. For the reconstruction of the cardic diffusion tensor field some of the mismatch between the results and the the original tensor field may be a harmonic tensor field of small magintude. We speculate that the same would be true for the reconstruction of a tensor field on a bounded domain, i.e., using our decomposition and algorithm would result in a non-uniqueness (missing part) of a constant homogeneous background of low intensity.

Work in vector tomography has also shown that if the constant attenuator of the scalar projections is known, then only longitudinal scalar projections in the direction of the projection angle [62] are required to reconstruct the vector field. Later Natterer [63] showed that transverse scalar projections would only be required; however, in practice these measurements can be difficult to acquire. Previously we investigated this for vector [64] and tensor [65] fields by simulating attenuated projections of scalar measurements around one orbit. The results indicated that the elements of the vectors are

recovered, whereas components of the tensor field are not fully recovered.

E. X-Ray Dark-Field Imaging

1) X-Ray Tensor Tomography (XTT): Of particular interest to us is the application of tensor tomography in X-ray dark-field imaging of fiber orientation in tissue. The X-ray tensor tomography (XTT) method [8], [66] divides the reconstruction of tensor fields into two steps: first to reconstruct coefficients of a Cartesian vector representation at each voxel; and then fit the estimated vector coefficients to an ellipsoidal representation of the second rank tensor at each voxel. The forward model represents the small-angle scatter as the discrete supposition of the anisotropic scatter signal, much like the Beer–Lambert model for the X-ray attenuation signal [66]. Vogel *et al.* [67] formulated the reconstruction of the ellipsoidal representation of the fixed basis set of vectors as a regular inverse problem whereby an iterative reconstruction algorithm is used to estimate vector coefficients constrained by an ellipsoidal function. Iterative approaches have advantages in addition to modeling noise, to provide constraints on the solution. A Bayesian approach adding constraints to XTT was pursued by [68] who proposed a cost function with regularization to iteratively reconstruct simultaneously attenuation, phase, and scatter images (with independent penalty functions) from differential phase contrast acquisitions, without the need of phase retrieval. In our work we performed simulations evaluating the model of [8], [67] with the reconstruction of coefficients for a fixed basis set of 7 vectors. The coefficients were reconstructed from Moiré fringe analysis of single-exposure dark-field projections obtained from X-ray bi-prism interferometry [69]. Wieczorek *et al.* [12] modified the forward model [8], [67] to develop an anisotropic X-ray dark-field tomography (AXDT) method by replacing the discretization of the scatter function as a fixed basis set of vectors at each voxel with a spherical harmonic expansion. They demonstrated signific differences in the results between XTT and AXDT in the small-angle scatter indicating that the spherical harmonic approach may be a more general representation of the small-angle scatter than the tensor approach. Early on a different forward model was proposed by Bayer *et al.* [9] where instead of a vector basis expansion; the isotropic scatter contribution, the anisotropic scatter contribution, and the in-plane scatter angel was modeled using a sinusoidal expansion where coefficients were reconstructed from X-ray dark-field projections using Talbot-Lau grating interferometry. More recently, Kim *et al.* [14] proposed the use of a periodic array of multi-circular gratings for Talbot-Lau interferometry instead of linear gratings to capture 2D-omnidirectional X-ray scattering signals within a single projection shot, removing the necessity of rotation of the sample relative to the gradient alignment. In this work vector coefficients were reconstructed following the model of Malecki *et al.* [8], [66].

2) Reciprocal Space Representation of X-Ray Scatter: Other groups investigated the possibility of directly reconstructing a q-vector representation of reciprocal space as a measure of the small-angle scatter (SAXS) from direct dark-field measurements using X-ray raster scanning [10], [11]. The use of raster scanning to measure small-angel X-ray scatter (SAXS) is a valuable imaging technique to obtain which q-vectors are probed for each projection. A virtual tomography axis is presented where projection-dependent rotation matrix describes the relationship between laboratory and sample coordination systems. Schaff *et al.* [13] later investigated the possibility of instead of using raster scanning, using XTT data obtained from Talbot-Lau X-ray grating interferometry to fit models of reciprocal space representation of small-angle scatter. Ellipsoids are fit to the reconstructed results. As with the use of spherical harmonics in real space representation of scatter, spherical harmonics were also used for the basis representation of q-vectors in reciprocal-space modeling of small-angle scatter from data obtained with X-ray raster scanning [10], [70]. To improve the speed of the reconstruction, a fast iterative back-projection reconstruction algorithm [46] was designed to directly reconstruct elements of a second rank tensor. This was the first tensor tomography approach to directly reconstruct elements of a second rank tensor representation of small-angle scatter from dark-field projections. The tensor representation of the projections was transverse corresponding to the direction of the sensitivity of the gratings.

3) Scatter as a Tensor: In many of these approaches the question arises as to whether sufficient data is obtained to uniquely reconstruct the coefficients of the models used to represent the small-angle scatter. We know from our work presented in this paper with that of using a filter back-projection algorithm, 3 orthogonal axes obtaining 6 sets of projections provide 6 independent equations to solve for the 6 unknows of a tensor representation of small-angle scatter. However, specific orientation dependence of small-angle scatter and the non-linear function of the underlying anisotropic mass distribution brings into question as to whether a tensor representation is a correct model of the anisotropic small angel scatter [15]. Graetz [15] investigated whether two approximative linear tensor models with reduced orientation dependence were applicable models of small-angle scatter for grating based X-ray or neutron dark-field tensor tomography. In so doing he showed that X-ray dark-field scatter could be approximated as a tensor and using X-ray interferometry, longitudinal and transverse directional measurements could form scalar directional tensor projections. Simulations verified that in using tomographic applications with full sampling over a sphere, these linear tensor models can recover orientations up to a statistical accuracy on the scale of 1°. However, if the tensor representation was reconstructed using only a minimal set of three circular acquisition trajectories, principal orientations for isolated volume elements could still be recovered to a statistical accuracy of 5° to 10°.

F. Magnetic Resonance Imaging

1) Diffusion Tensor Magnetic Resonance Imaging (DT-MRI): The application of tensor tomography in MR diffusion tensor imaging is more in question as to its applicability since most of MRI acquisition schemes (protocols, pulse sequences) acquire data that directly map Fourier space requiring no tomography, only an inverse 2D or 3D Fourier transform to

directly obtain the real space image. Even more changeling is the work in the last two decades in developing better diffusion models for brain tractography – where the brain covers a wide range of spatial scale of anatomy from global structure of white matter fiber tracts to microstructure of axons–that go beyond the tensor representation [71], [72]. Some of these methods are modification of the diffusion tensor model; here we present three examples: 1) Neurite Orientation Dispersion and Density Imaging (NODDI) distinguishes between intracellular, extracellular, and cerebrospinal fluid (CSF) compartments by assuming the diffusion signal is the sum of diffusion signals from multiple compartments [73]. Multi-compartment models are limited in modeling bending and fanning fiber configurations in a voxel and in determining the correct number of compartments [74]. 2) Diffusion Kurtosis imaging (DKI) is another class of methods aimed at using a fiber orientation distribution function (fODF) [75] to estimate a fiber orientation which is important for tractography and connective analysis by way of a diffusion orientation function (dODF). DKI is a statistical measure of the deviation from a Gaussian distribution [which is the assumed distribution for diffusion tensor imaging (DTI)], and thus, DKI provides a significantly more complete characterization of water diffusion and tissue structure. This technique is largely based on the same type of pulse sequences employed for DTI, but DKI requires multishell diffusion MRI (dMRI) at higher b values than those conventionally utilized for DTI analysis. 3) Q-space diffeomorphic reconstruction (QSDR). Other limitations of DTI relate to its inability to independently resolve crossing fibers and sensitivity to partial volume effects (PVE) as in studies using dODF to characterize the diffusion distribution. To overcome these effects, the spin distribution function (SDF) can be obtained from generalized Q-sampling imaging (GQI), where SDF represents the proportion of spins undergoing diffusion in different orientations. Notice this is like thecase with developing models of X-ray small-angle scatter, investigation of reciprocal space to obtain a q-space representations of small-angle scatter in tissue as a better model of small-angle scatter than a tensor representation. Q-space diffeomorphic reconstruction calculates the transformed SDFs in any given deformation field that satisfies diffeomorphism.To overcome some of these problems Karimi *et al.* [71] proposed to learn a direct mapping between the diffusion measurements in the q-space and the target fODF by using deep neural networks to learn the relationship between the DW-MRI signal and the fiber orientation distribution. The estimation of an fODF, on the other hand is sensitive to noise and prone to predicting false fibers, while other possible methods such as diffusion spectrum imaging (DSI) require a very large number of measurements that can lead to unrealistic scan times.

2) Diffusion Tensor Tomography Magnetic Resonance Imaging (DTT-MRI): Our previous work focused on developing diffusion tensor tomography magnetic resonance imaging (DTT-MRI) for the **heart**; one the most difficult organs to perform MR diffusion tensor imaging (MR-DTI) due to motion and the length of time required to obtain adequate images. For ex vivo samples we have acquired images for up to 12 hours on 3T small animal systems [76]. It can take a long time to acquire an MR diffusion tensor image of the heart with sufficient signal to noise, making it impractical for human imaging, though recent imaging times have significantly improved [19], [77]–[79]. For this reason, in our previous attempts to measure the heart fiber structure required in constructing mechanical models of the heart, we investigated ways of reducing the number of measurements (pulse repetitions), such as measuring and reconstructing only the principal eigenvectors in order to reduce the acquisition times but to provide some structural information of cardiac fiber structure [80]. With the hope that the heart fiber structure could be specified from its solenoidal tensor field, we also performed simulations of reconstructing solenoidal and irrotational images of a numerical helical heart phantom (representing a section of the mid-ventricular wall of the left ventricle) from scalar Radon projections (note: not X-ray projections) of the phantom [53]. Sampling projections around a single axis, we found Radon projections $\tilde{r}^{\alpha\,\alpha}_{\underline{\theta}}$, $\tilde{r}^{\alpha\,\beta}_{\underline{\theta}}$, and $\tilde{r}^{\beta\,\beta}_{\underline{\theta}}$ were needed for each projection $\underline{\theta}$ to reconstruct the three unknowns in the solenoidal tensor field and Radon projections $\tilde{r}^{\theta\,\theta}_{\underline{\theta}}$, $\tilde{r}^{\theta\,\alpha}_{\underline{\theta}}$, and $\tilde{r}^{\theta\,\beta}_{\underline{\theta}}$ were needed to reconstruct the three unknowns in the irrotational component of the tensor field [53]. In this work, we found that a realistic model of the helical fiber structure of the myocardial tissue specifies a diffusion tensor field for which the first principal vector (the vector associated with the maximum eigenvalue) of the solenoidal component accurately approximates the first principal vector of the diffusion tensor.

G. Summary

The second, third, and fourth rank tensors describe a wide range of physical phenomena with potential imaging applications. Second rank tensors are used to represent diffusivity [81], mechanical stress and strain [82], electromagnetic quantities [83] and physics related to gravity [84]. Third rank tensors have been used to describe the apparent bidirectional reflectance distribution function (BRDF) in face relighting applications [85]. Fourth rank tensors can approximate the diffusivity function from the DW-MRI data guaranteeing the symmetric positive-definite property [75]. Other applications include, X-ray strain imaging of crystals, specifically inverting the transverse ray transform of the projections of the diffraction pattern [51], neutron strain imaging of crystals [51], [86], photoelasticity strain imaging of crystals [87], travel time seismology studying the inner structure of the earth to determine the anisotropic index of refraction of the medium involving the mathematical challenge of determining a symmetric second rank tensor Riemannian metric from its integrals along geodesics [88]–[90], neutron tomography of magnetic vector fields in bulk materials [91], optical tomography of dielectric tensors [92], tomographical imaging of electrical and magnetic sources in brain and heart [93], [94], and tissue magnetic susceptibility tensor MR imaging [95].

In our previous work we performed simulations evaluating the reconstruction of the coefficients for a fixed basis set of 7 vectors from Moiré fringe analysis of projections of

a single-exposure of dark-field scatter obtained from X-ray bi-prism interferometry [69]. To obtain a tensor representation would have involved performing a second step of fitting the estimated vector coefficients to an ellipsoidal representation of the tensor at each voxel [8], [67]. In our simulations of this previous work, we used a wave optics approach to simulate the projections; whereas, in the present work we did not simulate a specific imaging modality but evaluated our filtered back-projection algorithm by numerically approximating the projections of a generic numerical tensor field and a diffusion tensor field of an excised human heart. Our future interests involve developing algorithms to directly reconstruct the tensor representation of small-angle scatter using X-ray bi-prism interferometry [96]. This interest is heightened by the fact that from the work of [15] it is appropriate to represent small-angle scatter as a second rank tensor of which one can measure longitudinal and transvers scalar projections of the tensor representation of small-angle scatter using X-ray dark-field imaging.

VII. Conclusion

We proposed a new filtered back-projection reconstruction algorithm to reconstruct tensor fields from projections acquired around three axes. Using a tensor field decomposition and Fourier projection theorem, we established relationships between the Fourier transform of the directional X-ray projection measurements and the Fourier transform of the solenoidal and irrotational components of the tensor field. A FBP algorithm was then derived to reconstruct the solenoidal and irrotational components from the directional X-ray transform of the tensor around three axes. The decomposition of the tensor field into solenoidal and irrotational components provides insight into the development of algorithms for emerging medical imaging technologies including the reconstruction of tensor fields with sufficient samples of directional projections and necessary orbits for the acquisition of projections for the tensor field.

Appendix
Tensor Field Decomposition

It was shown by Sharafutdinov [47], that a smooth symmetric tensor field which vanishes rapidly at infinity can be decomposed in a unique way as $t_{ij} = t^S_{ij}(\underline{x}) + \frac{1}{2}\left(\partial_i \phi_j(\underline{x}) + \partial_j \phi_i(\underline{x})\right)$, where $\underline{\phi}(\underline{x})$ is a vector potential that yields a curl free irrotational tensor field and $t^S_{ij}(\underline{x})$ is a symmetric solenoidal tensor field, which is divergence free: $\sum_i \partial_i t^S_{ij}(\underline{x}) = \sum_j \partial_j t^S_{ij}(\underline{x}) = 0$. If we take the Fourier transform, we see that $\sum_i \sigma_i \tilde{t}^S_{ij}(\underline{\sigma}) = \sum_j \sigma_j \tilde{t}^S_{ij}(\underline{\sigma}) = 0$.

In our paper we considered a similar decomposition, but explicitly specify the solenoidal component as a curl of a tensor potential as is done in the Helmholz vector field decomposition with a vector potential. We consider the following decomposition of a symmetric tensor field T:

$$T(\underline{x}) = T^S_\Psi(\underline{x}) + T^I_\Phi(\underline{x})$$

where the solenoidal component $T^S_\Psi(\underline{x})$ is a symmetric tensor and is divergence free and $T^I_\Phi(\underline{x})$ is a curl free symmetric tensor. We write the solenoidal component as $T^S_\Psi(\underline{x}) = \nabla \times \Psi(\underline{x})$, where

$$\Psi(\underline{x}) = \begin{bmatrix} \Psi_{xx} & \Psi_{xy} & \Psi_{xz} \\ \Psi_{yx} & \Psi_{yy} & \Psi_{yz} \\ \Psi_{zx} & \Psi_{zy} & \Psi_{zz} \end{bmatrix}(\underline{x}).$$

A correct interpretation of the curl of a second rank tensor is the vector curl operation applied to each column of Ψ, whereas the formal definition of the curl of a second rank tensor is [37], [61]

$$\nabla \times \Psi(\underline{x}) = \begin{bmatrix} \frac{\partial \Psi_{zx}}{\partial y} - \frac{\partial \Psi_{yx}}{\partial z} & \frac{\partial \Psi_{zy}}{\partial y} - \frac{\partial \Psi_{yy}}{\partial z} & \frac{\partial \Psi_{zz}}{\partial y} - \frac{\partial \Psi_{yz}}{\partial z} \\ \frac{\partial \Psi_{xx}}{\partial z} - \frac{\partial \Psi_{zx}}{\partial x} & \frac{\partial \Psi_{xy}}{\partial z} - \frac{\partial \Psi_{zy}}{\partial x} & \frac{\partial \Psi_{xz}}{\partial z} - \frac{\partial \Psi_{zz}}{\partial x} \\ \frac{\partial \Psi_{yx}}{\partial x} - \frac{\partial \Psi_{xx}}{\partial y} & \frac{\partial \Psi_{yy}}{\partial x} - \frac{\partial \Psi_{xy}}{\partial y} & \frac{\partial \Psi_{yz}}{\partial x} - \frac{\partial \Psi_{xz}}{\partial y} \end{bmatrix}(\underline{x}),$$

with elements defined by

$$t_{kl} = \sum_{i=1}^{3}\sum_{j=1}^{3} \nabla_i \Psi_{jl} \epsilon_{ijk},$$

where ε_{ijk}, as shown at the bottom of the next page, is the permutation tensor (Levi-Civita symbols): Next take the Fourier transform of $\nabla \times \Psi(\underline{x})$

$$\widetilde{\nabla \times \Psi}(\underline{\sigma}) = \begin{bmatrix} \sigma_y \tilde{\Psi}_{zx} - \sigma_z \tilde{\Psi}_{yx} & \sigma_y \tilde{\Psi}_{zy} - \sigma_z \tilde{\Psi}_{yy} & \sigma_y \tilde{\Psi}_{zz} - \sigma_z \tilde{\Psi}_{yz} \\ \sigma_z \tilde{\Psi}_{xx} - \sigma_x \tilde{\Psi}_{zx} & \sigma_z \tilde{\Psi}_{xy} - \sigma_x \tilde{\Psi}_{zy} & \sigma_z \tilde{\Psi}_{xz} - \sigma_x \tilde{\Psi}_{zz} \\ \sigma_x \tilde{\Psi}_{yx} - \sigma_y \tilde{\Psi}_{xx} & \sigma_x \tilde{\Psi}_{yy} - \sigma_y \tilde{\Psi}_{xy} & \sigma_x \tilde{\Psi}_{yz} - \sigma_y \tilde{\Psi}_{xz} \end{bmatrix} \times (\underline{\sigma}).$$

Divergence free: $\sum_i \partial_i t^S_{ij}(\underline{x}) = \sum_j \partial_j t^S_{ij}(\underline{x}) = 0$ implies $\sum_i \sigma_i \tilde{t}^S_{ij}(\underline{\sigma}) = \sum_j \sigma_j \tilde{t}^S_{ij}(\underline{\sigma}) = 0$ thus

$$\begin{aligned} &\sigma_x\left[\sigma_y \tilde{\Psi}_{zx} - \sigma_z \tilde{\Psi}_{yx}\right] + \sigma_y\left[\sigma_z \tilde{\Psi}_{xx} - \sigma_x \tilde{\Psi}_{zx}\right] \\ &\quad + \sigma_z\left[\sigma_x \tilde{\Psi}_{yx} - \sigma_y \tilde{\Psi}_{xx}\right] = 0 \\ &\Rightarrow \left[\sigma_y \sigma_z - \sigma_y \sigma_z\right] \tilde{\Psi}_{xx} = 0 \\ &\sigma_x\left[\sigma_y \tilde{\Psi}_{zy} - \sigma_z \tilde{\Psi}_{yy}\right] + \sigma_y\left[\sigma_z \tilde{\Psi}_{xy} - \sigma_x \tilde{\Psi}_{zy}\right] \\ &\quad + \sigma_z\left[\sigma_x \tilde{\Psi}_{yy} - \sigma_y \tilde{\Psi}_{xy}\right] = 0 \\ &\Rightarrow \left[\sigma_z \sigma_x - \sigma_x \sigma_z\right] \tilde{\Psi}_{yy} = 0 \\ &\sigma_x\left[\sigma_y \tilde{\Psi}_{zz} - \sigma_z \tilde{\Psi}_{yz}\right] + \sigma_y\left[\sigma_z \tilde{\Psi}_{xz} - \sigma_x \tilde{\Psi}_{zz}\right] \\ &\quad + \sigma_z\left[\sigma_x \tilde{\Psi}_{yz} - \sigma_y \tilde{\Psi}_{xz}\right] = 0 \\ &\Rightarrow \left[\sigma_x \sigma_y - \sigma_y \sigma_x\right] \tilde{\Psi}_{zz} = 0 \end{aligned}$$

If we choose $\tilde{\Psi}_{xx} = \tilde{\Psi}_{yy} = \tilde{\Psi}_{zz} = 0$ and $\widetilde{\nabla \times \Psi}(\underline{\sigma})$ is a symmtric tensor then

$$\begin{aligned} -\sigma_x \tilde{\Psi}_{zx} = \sigma_y \tilde{\Psi}_{zy} &\Rightarrow \tilde{\Psi}_{zx} = -\frac{\sigma_y}{\sigma_x}\tilde{\Psi}_{zy} \\ \sigma_x \tilde{\Psi}_{yx} = -\sigma_z \tilde{\Psi}_{yz} &\Rightarrow \tilde{\Psi}_{yx} = -\frac{\sigma_z}{\sigma_x}\tilde{\Psi}_{yz} \\ -\sigma_y \tilde{\Psi}_{xy} = \sigma_z \tilde{\Psi}_{xz} &\Rightarrow \tilde{\Psi}_{xy} = -\frac{\sigma_z}{\sigma_y}\tilde{\Psi}_{xz} \end{aligned}$$

$$\varepsilon_{ijk} = \begin{cases} +1 & (i,j,k) \text{ is an even permutation of indices} \\ -1 & (i,j,k) \text{ is an odd permutation of indices} \\ 0 & \text{otherwise} \end{cases}$$

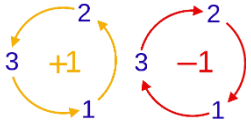

Choosing $\tilde{\Psi}_{xz} = -\sigma_y \tilde{X}_1$, $\tilde{\Psi}_{yz} = \sigma_x \tilde{X}_2$, $\tilde{\Psi}_{zy} = -\sigma_x \tilde{X}_3$, we obtain

$$\begin{aligned}
-\sigma_x \tilde{\Psi}_{zx} &= \sigma_y \tilde{\Psi}_{zy} \Rightarrow \tilde{\Psi}_{zx} = -\frac{\sigma_y}{\sigma_x}\left(-\sigma_x \tilde{X}_3\right) \\
\sigma_x \tilde{\Psi}_{yx} &= -\sigma_z \tilde{\Psi}_{yz} \Rightarrow \tilde{\Psi}_{yx} = -\frac{\sigma_z}{\sigma_x}\left(\sigma_x \tilde{X}_2\right) \\
-\sigma_y \tilde{\Psi}_{xy} &= \sigma_z \tilde{\Psi}_{xz} \Rightarrow \tilde{\Psi}_{xy} = -\frac{\sigma_z}{\sigma_y}\left(-\sigma_y \tilde{X}_1\right) \\
\tilde{\Psi}_{zx} &= -\frac{\sigma_y}{\sigma_x}\left(-\sigma_x \tilde{X}_3\right) = \sigma_y \tilde{X}_3 \\
\tilde{\Psi}_{yx} &= -\frac{\sigma_z}{\sigma_x}\left(-\sigma_x \tilde{X}_2\right) = -\sigma_z \tilde{X}_2 \\
\tilde{\Psi}_{xy} &= -\frac{\sigma_z}{\sigma_y}\left(-\sigma_y \tilde{X}_1\right) = \sigma_z \tilde{X}_1
\end{aligned}$$

With $\tilde{\Psi}_{xx} = \tilde{\Psi}_{yy} = \tilde{\Psi}_{zz} = 0$ and taking the inverse Fourier transform of the elements $\tilde{\Psi}_{ab}$, we have

$$\Psi(\underline{x}) = \begin{bmatrix} 0 & \frac{\partial X_1}{\partial z} & -\frac{\partial X_1}{\partial y} \\ -\frac{\partial X_2}{\partial z} & 0 & \frac{\partial X_2}{\partial x} \\ \frac{\partial X_3}{\partial y} & -\frac{\partial X_3}{\partial x} & 0 \end{bmatrix}(\underline{x}),$$

and

$$\begin{aligned}
T_\Psi^S(\underline{x}) &= \nabla \times \Psi(\underline{x}) \\
&= \begin{bmatrix} \frac{\partial^2 X_3}{\partial y^2} + \frac{\partial^2 X_2}{\partial z^2} & -\frac{\partial^2 X_3}{\partial y \partial x} & -\frac{\partial^2 X_2}{\partial z \partial x} \\ -\frac{\partial^2 X_3}{\partial x \partial y} & \frac{\partial^2 X_1}{\partial z^2} + \frac{\partial^2 X_3}{\partial x^2} & -\frac{\partial^2 X_1}{\partial z \partial y} \\ -\frac{\partial^2 X_2}{\partial x \partial z} & -\frac{\partial^2 X_1}{\partial y \partial z} & \frac{\partial^2 X_2}{\partial x^2} + \frac{\partial^2 X_1}{\partial y^2} \end{bmatrix}(\underline{x})
\end{aligned}$$

Note that $T_\Psi^S(\underline{x})$ is a symmetric divergence free tensor: $\sum_i \partial_i t_{ij}^S(\underline{x}) = \sum_j \partial_j t_{ij}^S(\underline{x}) = 0$, for example

$$\begin{aligned}
&\frac{\partial}{\partial x}\left[\frac{\partial^2 X_3}{\partial y^2} + \frac{\partial^2 X_2}{\partial z^2}\right] - \frac{\partial}{\partial y}\frac{\partial^2 X_3}{\partial y \partial x} - \frac{\partial}{\partial z}\frac{\partial^2 X_2}{\partial z \partial x} \\
&\qquad = \frac{\partial^3 X_3}{\partial x \partial y^2} + \frac{\partial^3 X_2}{\partial x \partial z^2} - \frac{\partial^3 X_3}{\partial y^2 \partial x} - \frac{\partial^3 X_2}{\partial z^2 \partial x} = 0.
\end{aligned}$$

REFERENCES

[1] J. Tromp, C. Tape, and Q. Liu, "Seismic tomography, adjoint methods, time reversal and banana-doughnut kernels," *Geophys. J. Int.*, vol. 160, no. 1, pp. 195–216, Dec. 2004.

[2] F. Hofmann *et al.*, "Nanoscale imaging of the full strain tensor of specific dislocations extracted from a bulk sample," *Phys. Rev. Mater.*, vol. 4, no. 1, p. 013801, 2020.

[3] G. P. Paternain, M. Salo, and G. Uhlmann, "Tensor tomography on surfaces," *Inventiones mathematicae*, vol. 193, no. 1, pp. 229–247, Jul. 2013.

[4] A. L. Alexander, J. E. Lee, M. Lazar, and A. S. Field, "Diffusion tensor imaging of the brain," *Neurotherapeutics*, vol. 4, no. 3, pp. 316–329, 2007.

[5] H. Einarsdóttir *et al.*, "Computer-aided diagnosis of pulmonary diseases using X-ray darkfield radiography," *Phys. Med. Biol.*, vol. 60, no. 24, p. 9253, 2015.

[6] T. Baum *et al.*, "X-ray dark-field vector radiography—A novel technique for osteoporosis imaging," *J. Comput. Assist. Tomogr.*, vol. 39, no. 2, pp. 286–289, 2015.

[7] S. T. Taba, T. E. Gureyev, M. Alakhras, S. Lewis, D. Lockie, and P. C. Brennan, "X-ray phase-contrast technology in breast imaging: Principles, options, and clinical application," *Amer. J. Roentgenology*, vol. 211, no. 1, pp. 133–145, Jul. 2018.

[8] A. Malecki *et al.*, "X-ray tensor tomography," *EPL (Europhys. Lett.)*, vol. 105, no. 3, p. 38002, 2014.

[9] F. L. Bayer *et al.*, "Reconstruction of scalar and vectorial components in X-ray dark-field tomography," *Proc. Nat. Acad. Sci. USA*, vol. 111, no. 35, pp. 12699–12704, 2014.

[10] M. Liebi *et al.*, "Nanostructure surveys of macroscopic specimens by small-angle scattering tensor tomography," *Nature*, vol. 527, no. 7578, pp. 349–352, Nov. 2015.

[11] F. Schaff *et al.*, "Six-dimensional real and reciprocal space small-angle X-ray scattering tomography," *Nature*, vol. 527, no. 7578, pp. 353–356, Nov. 2015.

[12] M. Wieczorek, F. Schaff, F. Pfeiffer, and T. Lasser, "Anisotropic X-ray dark-field tomography: A continuous model and its discretization," *Phys. Rev. Lett.*, vol. 117, no. 15, Oct. 2016, Art. no. 158101.

[13] F. Schaff, F. Prade, Y. Sharma, M. Bech, and F. Pfeiffer, "Non-iterative directional dark-field tomography," *Sci. Rep.*, vol. 7, no. 1, pp. 1–9, Dec. 2017.

[14] J. Kim, M. Kagias, F. Marone, and M. Stampanoni, "X-ray scattering tensor tomography with circular gratings," *Appl. Phys. Lett.*, vol. 116, no. 13, Mar. 2020, Art. no. 134102.

[15] J. Graetz, "Simulation study towards quantitative X-ray and neutron tensor tomography regarding the validity of linear approximations of dark-field anisotropy," *Sci. Rep.*, vol. 11, no. 1, pp. 1–11, Dec. 2021.

[16] M. J. Moulton, B. D. Hong, and T. W. Secomb, "Simulation of left ventricular dynamics using a low-order mathematical model," *Cardiovascular Eng. Technol.*, vol. 8, no. 4, pp. 480–494, Dec. 2017.

[17] M. Froeling, G. J. Strijkers, A. J. Nederveen, S. A. Chamuleau, and P. R. Luijten, "Diffusion tensor MRI of the heart–*in vivo* imaging of myocardial fiber architecture," *Current Cardiovascular Imag. Rep.*, vol. 7, no. 7, p. 9276, 2014.

[18] A. Das *et al.*, "The effect of microvascular obstruction on the myocardial microstructure: A diffusion tensor imaging study," *Eur. Heart J.-Cardiovascular Imag.*, vol. 22, Jan. 2021, Art. no. jeaa356.

[19] S. R. Watson, J. D. Dormer, and B. Fei, "Imaging technologies for cardiac fiber and heart failure: A review," *Heart Failure Rev.*, vol. 23, no. 2, pp. 273–289, Mar. 2018.

[20] V. Talman and H. Ruskoaho, "Cardiac fibrosis in myocardial infarction-from repair and remodeling to regeneration," *Cell Tissue Res.*, vol. 365, no. 3, pp. 563–581, 2016.

[21] D. M. Kramer and P. C. Lauterbur, "On the problem of reconstructing images of non-scalar parameters from projections. Application to vector fields," *IEEE Trans. Nucl. Sci.*, vol. 26, no. 2, pp. 2674–2677, Apr. 1979.

[22] S. J. Norton, "Tomographic reconstruction of 2-D vector fields: Application to flow imaging," *Geophys. J. Int.*, vol. 97, no. 1, pp. 161–168, Apr. 1989.

[23] K. B. Winters and D. Rouseff, "A filtered backprojection method for the tomographic reconstruction of fluid vorticity," *Inverse Problems*, vol. 6, no. 4, pp. L33–L38, Aug. 1990.

[24] H. Braun and A. Hauck, "Tomographic reconstruction of vector fields," *IEEE Trans. Signal Process.*, vol. 39, no. 2, pp. 464–471, Feb. 1991.

[25] S. J. Norton, "Unique tomographic reconstruction of vector fields using boundary data," *IEEE Trans. Image Process.*, vol. 1, no. 3, pp. 406–412, Jul. 1992.

[26] S. Juhlin, "Doppler tomography the IEEE Engineering in Medicine and Biology Society," in *Proc. 15th Annu. Int. Conf. IEEE*, 1993, pp. 212–213.

[27] G. Sparr, K. Strahlen, K. Lindstrom, and H. W. Persson, "Doppler tomography for vector fields," *Inverse Problems*, vol. 11, no. 5, p. 1051, 1995.

[28] A. Denisov, A. Popov, and V. Sterlyadkin, "Doppler tomography problem for a two-dimensional vector field," *Moscow Univ. Comput. Math. Cybern.*, vol. 1, pp. 17–20, Mar. 1995.

[29] L. Desbat and A. Wernsdorfer, "Direct algebraic reconstruction and optimal sampling in vector field tomography," *IEEE Trans. Signal Process.*, vol. 43, no. 8, pp. 1798–1808, Aug. 1995.

[30] J. L. Prince, "Convolution backprojection formulas for 3-D vector tomography with application to MRI," *IEEE Trans. Image Process.*, vol. 5, no. 10, pp. 1462–1472, Oct. 1996.

[31] G. Sparr and K. Strahlen, "Vector field tomography: An overview," in *IMA Volumes in Mathematics and its Applications; Computational Radiology and Imaging: Therapy and Diagnostic*, vol. 110. 1998.

[32] T. Schuster, "The 3D Doppler transform: Elementary properties and computation of reconstruction kernels," *Inverse Problems*, vol. 16, no. 3, pp. 701–723, 2000.

[33] T. Schuster, "An efficient mollifier method for three-dimensional vector tomography: Convergence analysis and implementation," *Inverse Problems*, vol. 17, no. 4, pp. 739–766, Aug. 2001.

[34] V. Sharafutdinov, "Slice-by-slice reconstruction algorithm for vector tomography with incomplete data," *Inverse Problems*, vol. 23, no. 6, p. 2603, 2007.

[35] Y. Censor, M. Jiang, and A. K. Louis, *Mathematical Methods in Biomedical Imaging and Intensity-Modulated Radiation Therapy (IMRT)* (Scuola Normale Superiore Edizioni della Normale), 2008.

[36] A. K. Louis, S. V. Maltseva, A. P. Polyakova, T. Schuster, and I. E. Svetov, "On solving the slice-by-slice three-dimensional 2-tensor tomography problems using the approximate inverse method," in *Proc. J. Phys., Conf.*, vol. 1715, 2021, Art. no. 012036.

[37] G. T. Gullberg, D. G. Roy, G. L. Zeng, A. L. Alexander, and D. L. Parker, "Tensor tomography," *IEEE Trans. Nucl. Sci.*, vol. 46, no. 4, pp. 991–1000, Aug. 1999.

[38] G. T. Gullberg and M. Defrise, "Three-dimensional tomography for vector and tensor fields," in *Proc. Int. Meeting Fully Three-Dimensional Image Reconstruction Radiol. Nucl. Med.*, 1999, pp. 369–372.

[39] G. T. Gullberg, M. Defrise, V. Y. Panin, and G. L. Zeng, "Backprojection filtering algorithms for reconstruction of vector and second order tensor fields," in *Proc. IEEE Nucl. Sci. Symp. Conf. Rec.*, vol. 2, Oct. 2000, pp. 277–281.

[40] M. Defrise and G. T. Gullberg, "3D reconstruction of tensors and vectors," Office Sci. Tech. Inf., Tech. Rep., 2005.

[41] A. Denisjuk, "Inversion of the X-ray transform for 3D symmetric tensor fields with sources on a curve," *Inverse Problems*, vol. 22, no. 2, pp. 399–411, Apr. 2006.

[42] W. Lionheart and V. Sharafutdinov, "Reconstruction algorithm for the linearized polarization tomography problem with incomplete data," *Contemp. Math.*, vol. 14, p. 137, Sep. 2009.

[43] N. M. Desai and W. R. B. Lionheart, "An explicit reconstruction algorithm for the transverse ray transform of a second rank tensor field from three axis data," *Inverse Problems*, vol. 32, no. 11, Nov. 2016, Art. no. 115009.

[44] E. Y. Derevtsov, A. K. Louis, S. V. Maltseva, A. P. Polyakova, and I. E. Svetov, "Numerical solvers based on the method of approximate inverse for 2D vector and 2-tensor tomography problems," *Inverse Problems*, vol. 33, no. 12, Dec. 2017, Art. no. 124001.

[45] R. Bammer, S. J. Holdsworth, W. B. Veldhuis, and S. T. Skare, "New methods in diffusion-weighted and diffusion tensor imaging," *Magn. Reson. Imag. Clinics North Amer.*, vol. 17, no. 2, pp. 175–204, May 2009.

[46] Z. Gao, M. Guizar-Sicairos, V. Lutz-Bueno, A. Schrter, and M. Georgiadis, "High-speed tensor tomography: Iterative reconstruction tensor tomography (IRTT) algorithm," *Acta Crystallographica A, Found. Adv.*, vol. 75, no. 2, pp. 223–238, 2019.

[47] V. A. Sharafutdinov, *Integral Geometry of Tensor Fields* (Inverse and Ill-Posed Problems Series). 1994.

[48] G.-R. Wang, "A Cramer rule for minimum-norm (T) least-squares (S) solution of inconsistent linear equations," *Linear Algebra Appl.*, vol. 74, pp. 213–218, Feb. 1986.

[49] H. Stark, J. W. Woods, I. Paul, and R. Hingorani, "Direct Fourier reconstruction in computer tomography," *IEEE Trans. Acoust., Speech, Signal Process.*, vol. 29, no. 2, pp. 237–245, Apr. 1981.

[50] D. Rohmer, A. Sitek, and G. T. Gullberg, "Reconstruction and visualization of fiber and laminar structure in the normal human heart from *ex vivo* diffusion tensor magnetic resonance imaging (DTMRI) data," *Investigative Radiol.*, vol. 42, no. 11, pp. 777–789, 2006.

[51] W. R. B. Lionheart and P. J. Withers, "Diffraction tomography of strain," *Inverse Problems*, vol. 31, no. 4, Apr. 2015, Art. no. 045005.

[52] P. B. Kingsley, "Introduction to diffusion tensor imaging mathematics: Part III. Tensor calculation, noise, simulations, and optimization," *Concepts Magn. Reson. A*, vol. 28A, no. 2, pp. 155–179, 2006.

[53] G. T. Gullberg, M. Defrise, V. Y. Panin, and G. L. Zeng, "Efficient cardiac diffusion tensor MRI by three-dimensional reconstruction of solenoidal tensor fields," *Magn. Reson. Imag.*, vol. 19, no. 2, pp. 233–256, Feb. 2001.

[54] E. Y. Derevtsov and I. Svetov, "Tomography of tensor fields in the plain," *Eurasian J. Math. Comput. Appl.*, vol. 3, no. 2, pp. 24–68, 2015.

[55] A. Polyakova and B. M. Hahn, "A solution of the dynamic two-dimensional 2-tensor tomography problem using the SVD-method," *Frontier Math. Comput. Sci.*, vol. 12, p. 82, Aug. 2020.

[56] A. K. Louis and P. Maass, "A mollifier method for linear operator equations of the first kind," *Inverse Problems*, vol. 6, no. 3, p. 427, 1990.

[57] G. B. Arfken and H.-J. Weber, *Mathematical Methods for Physicists*. San Diego, CA, USA: Academic Harcourt Brace Jovanovich, 1967.

[58] A. Polyakova and I. Svetov, "The singular value decomposition of the dynamic ray transforms operators acting on 2-tensor fields in R^2," in *Proc. J. Phys., Conf.*, vol. 2021, vol. 1715, no. 1, Art. no. 012040.

[59] N. F. Osman and J. L. Prince, "3D vector tomography on bounded domains," *Inverse Problems*, vol. 14, no. 1, p. 185, 1998.

[60] T. McGraw, T. Kawai, I. Yassine, and L. Zhu, "New scalar measures for diffusion-weighted MRI visualization," in *Proc. Int. Symp. Vis. Comput.* Berlin, Germany: Springer, 2009, pp. 934–943.

[61] T. McGraw, T. Kawai, I. Yassine, and L. Zhu, "Visualizing high-order symmetric tensor field structure with differential operators," *J. Appl. Math.*, vol. 2011, Jul. 2011, Art. no. 142923.

[62] A. A. Bukhgeim and S. G. Kazantsev, "Full reconstruction of a vector field from its attenuated vectorial radon transform," in *Modelling, Identification and Control*. 2003, pp. 294–298.

[63] F. Natterer, "Inverting the attenuated vectorial radon transform," *J. Inverse Ill-Posed Problems*, vol. 13, no. 1, pp. 93–101, Jan. 2005.

[64] Q. Huang, "Attenuated vector tomography–An approach to image flow vector fields with Doppler ultrasonic imaging," Tech. Rep., 2008.

[65] Q. Huang and G. T. Gullberg, "Attenuation corrected tensor tomography–attenuation helps in the case of insufficient measurements," in *Proc. IEEE Nucl. Sci. Symp. Conf. Rec.*, vol. 6, Oct./Nov. 2007, pp. 4103–4109.

[66] A. Malecki, "X-ray tensor tomography," Ph.D. thesis, Dept. Phys., Inst. Med. Eng., Tech. Univ. München, Munich, Germany, 2014.

[67] J. Vogel *et al.*, "Constrained X-ray tensor tomography reconstruction," *Opt. Exp.*, vol. 23, no. 12, pp. 15134–15151, 2015.

[68] B. Brendel, M. von Teuffenbach, P. B. Noël, F. Pfeiffer, and T. Koehler, "Penalized maximum likelihood reconstruction for X-ray differential phase-contrast tomography," *Med. Phys.*, vol. 43, no. 1, pp. 188–194, 2016.

[69] W. Tao *et al.*, "Tomography of dark-field scatter including single-exposure Moiré fringe analysis with X-ray biprism interferometry—A simulation study," *Med. Phys.*, vol. 48, no. 10, pp. 6293–6311, 2021.

[70] M. Liebi *et al.*, "Small-angle X-ray scattering tensor tomography: Model of the three-dimensional reciprocal-space map, reconstruction algorithm and angular sampling requirements," *Acta Crystallographica A, Found. Adv.*, vol. 74, no. 1, pp. 12–24, Jan. 2018.

[71] D. Karimi, L. Vasung, C. Jaimes, F. Machado-Rivas, S. K. Warfield, and A. Gholipour, "Learning to estimate the fiber orientation distribution function from diffusion-weighted MRI," *NeuroImage*, vol. 239, Oct. 2021, Art. no. 118316.

[72] Y. Masutani, "Recent advances in parameter inference for diffusion MRI signal models," *Magn. Reson. Med. Sci.*, vol. 21, no. 1, pp. 132–147, 2022.

[73] M. Bergamino, E. G. Keeling, V. R. Mishra, A. M. Stokes, and R. R. Walsh, "Assessing white matter pathology in early-stage Parkinson disease using diffusion MRI: A systematic review," *Frontiers Neurol.*, vol. 11, p. 314, May 2020.

[74] B. Jeurissen, A. Leemans, J.-D. Tournier, D. K. Jones, and J. Sijbers, "Investigating the prevalence of complex fiber configurations in white matter tissue with diffusion magnetic resonance imaging," *Hum. Brain Mapping*, vol. 34, no. 11, pp. 2747–2766, Nov. 2013.

[75] A. Barmpoutis, M. S. Hwang, D. Howland, J. R. Forder, and B. C. Vemuri, "Regularized positive-definite fourth order tensor field estimation from DW-MRI," *NeuroImage*, vol. 45, no. 1, pp. S153–S162, Mar. 2009.

[76] N. Tran, A. Giannakidis, G. T. Gullberg, and Y. Seo, "Quantitative analysis of hypertrophic myocardium using diffusion tensor magnetic resonance imaging," *J. Med. Imag.*, vol. 3, no. 4, 2016, Art. no. 046001.

[77] S. Nielles-Vallespin, A. Scott, P. Ferreira, Z. Khalique, D. Pennell, and D. Firmin, "Cardiac diffusion: Technique and practical applications," *J. Magn. Reson. Imag.*, vol. 52, no. 2, pp. 348–368, Aug. 2020.

[78] Z. Khalique, P. F. Ferreira, A. D. Scott, S. Nielles-Vallespin, D. N. Firmin, and D. J. Pennell, "Diffusion tensor cardiovascular magnetic resonance imaging: A clinical perspective," *JACC: Cardiovascular Imag.*, vol. 13, no. 5, pp. 1235–1255, 2020.

[79] S. Paddock *et al.*, "Clinical translation of three-dimensional scar, diffusion tensor imaging, four-dimensional flow, and quantitative perfusion in cardiac MRI: A comprehensive review," *Frontiers Cardiovascular Med.*, vol. 8, p. 670, Jul. 2021.

[80] V. Y. Panin, G. L. Zeng, M. Defrise, and G. T. Gullberg, "Diffusion tensor MR imaging of principal directions: A tensor tomography approach," *Phys. Med. Biol.*, vol. 47, no. 15, p. 2737, 2002.

[81] E. Özarslan and T. H. Mareci, "Generalized diffusion tensor imaging and analytical relationships between diffusion tensor imaging and high angular resolution diffusion imaging," *Magn. Reson. Med.*, vol. 50, no. 5, pp. 955–965, Oct. 2003.

[82] T. Chung, *Applied Continuum Mechanics*. Cambridge, U.K.: Cambridge Univ. Press, 1996.

[83] A. Kovetz, *Electromagnetic Theory*. Oxford, U.K.: Oxford Univ. Press, 2000.

[84] S. M. Carroll, *An Introduction to General Relativity: Spacetime and Geometry*, vol. 101. Reading, MA, USA: Addison-Wesley, 2004, p. 102.

[85] R. Kumar, A. Barmpoutis, A. Banerjee, and B. C. Vemuri, "Non-lambertian reflectance modeling and shape recovery of faces using tensor splines," *IEEE Trans. Pattern Anal. Mach. Intell.*, vol. 33, no. 3, pp. 533–567, Mar. 2011.

[86] B. Abbey, S. Y. Zhang, W. Vorster, and A. M. Korsunsky, "Reconstruction of axisymmetric strain distributions via neutron strain tomography," *Nucl. Instrum. Methods Phys. Res. B, Beam Interact. Mater. At.*, vol. 270, pp. 28–35, Jan. 2012.

[87] D. D. Karov and A. E. Puro, "Tensor tomography of stresses in cubic single crystals," *Petersburg Polytech. Univ. J., Phys. Math.*, vol. 1, no. 1, pp. 24–28, 2015.

[88] M. Salo and G. Uhlmann, "The attenuated ray transform on simple surfaces," *J. Differ. Geometry*, vol. 88, no. 1, pp. 161–187, May 2011.

[89] G. P. Paternain, M. Salo, and G. Uhlmann, "Tensor tomography: Progress and challenges," 2013, *arXiv:1303.6114*.

[90] P. Stefanov, G. Uhlmann, A. Vasy, and H. Zhou, "Travel time tomography," *Acta Math. Sinica, English*, vol. 35, no. 6, pp. 1085–1114, 2019.

[91] A. Hilger, I. Manke, N. Kardjilov, M. Osenberg, H. Markötter, and J. Banhart, "Tensorial neutron tomography of three-dimensional magnetic vector fields in bulk materials," *Nature Commun.*, vol. 9, no. 1, pp. 1–7, Dec. 2018.

[92] H. Hammer and W. R. Lionheart, "Reconstruction of spatially inhomogeneous dielectric tensors through optical tomography," *J. Opt. Soc. Amer. A, Opt. Image Sci.*, vol. 22, no. 2, pp. 250–255, 2005.

[93] D. S. Tuch, V. J. Wedeen, A. M. Dale, J. S. George, and J. W. Belliveau, "Conductivity tensor mapping of the human brain using diffusion tensor MRI," *Proc. Nat. Acad. Sci. USA*, vol. 98, no. 20, pp. 11697–11701, Sep. 2001.

[94] Z. Hu, K. Ye, M. Bai, Z. Yang, and Q. Lin, "Solving the magnetocardiography forward problem in a realistic three-dimensional heart-torso model," *IEEE Access*, vol. 9, pp. 107095–107103, 2021.

[95] D. Pavlovic, S. Pekic, M. Stojanovic, and V. Popovic, "Traumatic brain injury: Neuropathological, neurocognitive and neurobehavioral sequelae," *Pituitary*, vol. 22, no. 3, pp. 270–282, Jun. 2019.

[96] G. T. Gullberg, U. Shrestha, S. J. W. Kim, Y. Seo, and M. Fuller, "X-ray bi-prism interferometry—A design study of proposed novel hardware," *Med. Phys.*, vol. 48, no. 10, pp. 6508–6523, 2021.